Article

Molecular Cell

Molecular Basis for SMC Rod Formation and Its Dissolution upon DNA Binding

Graphical Abstract

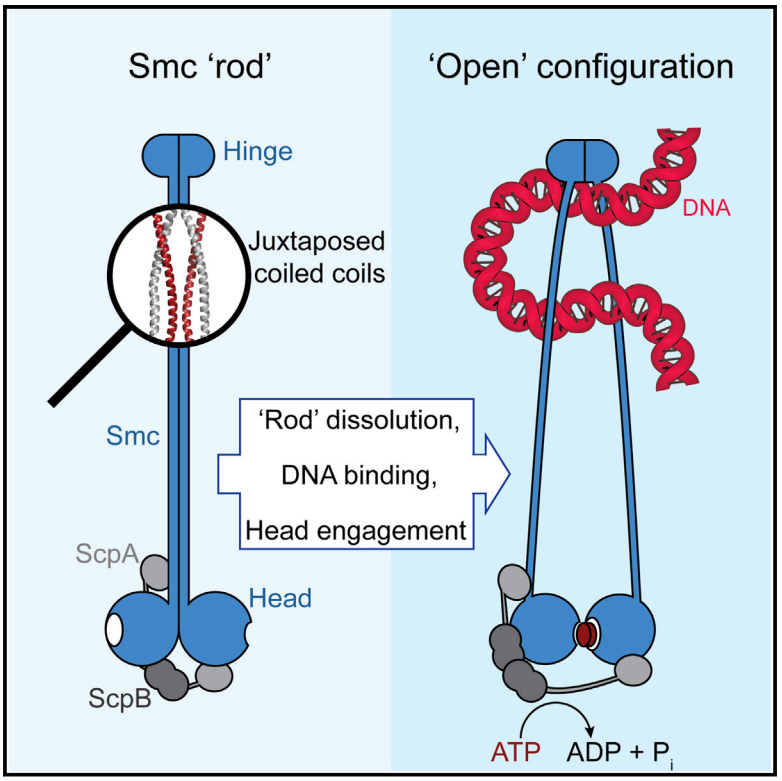

Authors

Young-Min Soh, Frank Bürmann, ..., Byung-Ha Oh, Stephan Gruber

Correspondence

bhoh@kaist.ac.kr (B.-H.O.), sgruber@biochem.mpg.de (S.G.)

In Brief

Soh et al. show that the rod-like conformation is a conserved architectural scheme of SMC complexes. Upon ATP-induced binding to DNA, the juxtaposed coiled coils of prokaryotic Smc-ScpAB adopt an open conformation to expose a DNA binding site at the inner surface of the hinge domain.

Highlights

- Prokaryotic Smc-ScpAB complexes form rod-like structures
- Binding of ATP and DNA induces a rod-to-ring transition in prokaryotic condensin
- The condensin hinge is rigidly anchored to its coiled coil
- The rod-like conformation is a conserved feature of SMC protein dimers

Soh et al., 2015, Molecular Cell *57*, 290–303
January 22, 2015
http://dx.doi.org/10.1016/j.molcel.2014.11.023

CellPress

CellPress

Molecular Cell
Article

Molecular Basis for SMC Rod Formation and Its Dissolution upon DNA Binding

Young-Min Soh,[1,7] Frank Bürmann,[2,7] Ho-Chul Shin,[1] Takashi Oda,[3] Kyeong Sik Jin,[4] Christopher P. Toseland,[2] Cheolhee Kim,[5] Hansol Lee,[1] Soo Jin Kim,[6] Min-Seok Kong,[1] Marie-Laure Durand-Diebold,[2] Yeon-Gil Kim,[4] Ho Min Kim,[6] Nam Ki Lee,[5] Mamoru Sato,[3] Byung-Ha Oh,[1,*] and Stephan Gruber[2,*]

[1]Department of Biological Sciences, KAIST Institute for the Biocentury, Cancer Metastasis Control Center, Korea Advanced Institute of Science and Technology, Daejeon 305-701, Korea
[2]Chromosome Organisation and Dynamics, Max Planck Institute of Biochemistry, Am Klopferspitz 18, 82152 Martinsried, Germany
[3]Graduate School of Medical Life Science, Yokohama City University, 1-7-29 Suehiro-cho, Tsurumi-ku, Yokohama, Kanagawa 230-0045, Japan
[4]Pohang Accelerator Laboratory, Pohang University of Science and Technology, Pohang, Kyungbuk, 790-784, Korea
[5]Department of Physics, Pohang University of Science and Technology, Pohang, Kyungbuk 790-784, Korea
[6]Graduate School of Medical Science and Engineering, Korea Advanced Institute of Science and Technology, Daejeon 305-701, Korea
[7]Co-first author
*Correspondence: bhoh@kaist.ac.kr (B.-H.O.), sgruber@biochem.mpg.de (S.G.)
http://dx.doi.org/10.1016/j.molcel.2014.11.023

SUMMARY

SMC condensin complexes are central modulators of chromosome superstructure in all branches of life. Their SMC subunits form a long intramolecular coiled coil, which connects a constitutive "hinge" dimerization domain with an ATP-regulated "head" dimerization module. Here, we address the structural arrangement of the long coiled coils in SMC complexes. We unequivocally show that prokaryotic Smc-ScpAB, eukaryotic condensin, and possibly also cohesin form rod-like structures, with their coiled coils being closely juxtaposed and accurately anchored to the hinge. Upon ATP-induced binding of DNA to the hinge, however, Smc switches to a more open configuration. Our data suggest that a long-distance structural transition is transmitted from the Smc head domains to regulate Smc-ScpAB's association with DNA. These findings uncover a conserved architectural theme in SMC complexes, provide a mechanistic basis for Smc's dynamic engagement with chromosomes, and offer a molecular explanation for defects in Cornelia de Lange syndrome.

INTRODUCTION

Chromosome condensation takes place in all forms of life. It is essential for faithful partitioning of replicated chromosomes into nascent daughter cells during cell division. Multisubunit complexes, termed condensins, are key mediators of this process (Hirano, 2012; Thadani et al., 2012). They commonly have a large core subunit (>1,100 amino acids) that belongs to the family of structural maintenance of chromosome proteins (SMC; in capital letters, used as a generic term for protein family). Several types of condensins have been identified: three condensins in prokaryotes, Smc-ScpAB, MukBEF, and MksBEF; and two eukaryotic condensins, condensin I and condensin II (condensin I/II). Smc-ScpAB comprises a homodimer of Smc and the two non-SMC subunits ScpA and ScpB (Mascarenhas et al., 2002; Soppa et al., 2002), whereas MukBEF comprises a homodimer of the SMC subunit MukB and the two non-SMC subunits MukE and MukF (Woo et al., 2009; Yamazoe et al., 1999). Smc-ScpAB is nearly ubiquitous in prokaryotes and more closely related to condensin in eukaryotes than MukBEF, which is found in only some branches of γ-proteobacteria. Condensin I/II are composed of the same heterodimer of Smc2 and Smc4 (Smc2-4) and a different set of three non-SMC subunits (Onn et al., 2007).

The SMC subunit exhibits a peculiar folding pattern: the extreme N- and C-terminal segments together form an ABC-type nucleotide binding domain (also called SMC head), a middle segment folds into a so-called hinge domain, and the two intervening segments form an ~50-nm-long antiparallel coiled coil connecting the two domains (Nolivos and Sherratt, 2014). The hinge domain is the interaction interface for the homo- or heterodimerization of SMC subunits (Haering et al., 2002). One of the non-SMC subunits generally belongs to a superfamily of proteins called kleisins, which bind and bridge the head domains of the SMC subunits (Schleiffer et al., 2003). In Smc-ScpAB condensin, the kleisin subunit ScpA binds two distinct interfaces on and near the Smc head domain to form a 1:1 asymmetric holocomplex between the Smc dimer and the $ScpA_1B_2$ subcomplex (Bürmann et al., 2013). Likewise, in condensin I/II, the head domains of the Smc2-4 heterodimer are presumably bridged by the kleisin subunit Cap-H/H2 that associates with two additional subunits, Cap-G/G2 and Cap-D2/D3 (Hirano, 2012).

The eukaryotic Smc1-Smc3 (Smc1-3) cohesin complex, which is evolutionarily related to condensin, is a chromosome concatenase that holds sister chromatid DNA within its closed ring structure (Nasmyth, 2011). Striking architectural similarities between different SMC complexes suggest that they all function

using a fundamentally conserved mode of action (Bürmann et al., 2013). Consistent with this notion, eukaryotic condensin, like cohesin, associates with minichromosomes by entrapment of DNA within its ring (Cuylen et al., 2011).

The distant hinge and head domains are involved in the loading of SMC-kleisin complexes onto DNA. ATP hydrolysis by Smc1 and Smc3 head domains is essential for stable binding of cohesin to chromosomes, whereas the SMC hinge domains harbor affinity for DNA in cohesin, condensin, and *Bacillus subtilis* (*Bs*) Smc-ScpAB (Arumugam et al., 2003; Chiu et al., 2004; Griese et al., 2010; Hirano and Hirano, 2006; Weitzer et al., 2003). DNA binding stimulates ATP hydrolysis in Smc-ScpAB and condensin in vitro (Hirano and Hirano, 2006; Kimura and Hirano, 1997), and hinge opening appears to be required for loading DNA into cohesin rings (Gruber et al., 2006). Whether (and how) ATP binding and hydrolysis at the SMC heads might be mechanistically coordinated with DNA binding to the hinge and opening of the DNA entry gate is largely unclear. Conceivably, the coiled-coil arms could provide a mechanical link if they were somewhat stiff and rigidly connected to hinge and/or head domains. According to electron microscopy (EM) and atomic force microscopy, the coiled coils in SMC dimers and SMC holocomplexes are not in random conformations but mostly V or O shaped or juxtaposed onto each other over their entire length (Anderson et al., 2002; Fuentes-Perez et al., 2012; Haering et al., 2002; Matoba et al., 2005; Melby et al., 1998). In the crystal structure of the *Thermotoga maritima* (*Tm*) Smc hinge, two short coiled coils protrude from the hinge domain dimer in nearly opposite orientations (Haering et al., 2002). Similar coiled-coil configurations were found in crystal structures of the MukB hinge domain (Ku et al., 2010; Li et al., 2010; Vos et al., 2013). The observed variety in the conformations of SMC coiled coils might be partly, or entirely, due to (1) intrinsic structural flexibility, (2) structural differences between classes of SMC-kleisin complexes, or (3) experimental artifacts. Thus, it is largely unclear what configurations SMC-kleisin rings adopt on the chromosome, or in solution, and whether conformational changes are required during chromosomal loading and unloading cycles.

Using an integrative approach including crystallographic analyses of SMC protein fragments with long stretches of coiled coil, we demonstrate that both prokaryotic and eukaryotic condensins form rod-shaped holocomplexes with rigid and juxtaposed coiled coils. We further reveal that binding of DNA to Smc dimers is incompatible with the reported coiled-coil arrangement at the hinge and uncover an interplay between DNA and ATP binding in the dynamic control of Smc arm conformation. These findings allow us to propose a mechanism by which the ATPase head domains regulate DNA binding to the hinge via engagement and disengagement of Smc coiled coils.

RESULTS

EM of Smc-ScpAB Holocomplexes

Crystallographic studies supported by biochemical and genetic data have provided detailed insights into the structures of all globular parts of prokaryotic Smc-ScpAB complexes. However, our understanding of the overall architecture of Smc-ScpAB and, in particular, the arrangement of the Smc coiled coils in the holocomplex of Smc-ScpAB has remained rather limited so far. Here, we have purified *Bs* Smc protein as well as Smc-ScpAB holocomplexes produced in *Escherichia coli* (*Ec*). As determined by size exclusion chromatography-multiangle light scattering (SEC-MALS), our preparations comprise near homogenous solutions with molecular weights fitting well to isolated Smc dimers and heteropentameric Smc_2-$ScpA_1B_2$ complexes (Figure S1 available online). The proteins were negatively stained and visualized by EM (Figures 1A and 1B). Smc dimers and Smc-ScpAB holocomplexes were almost exclusively detected as straight objects comprising a single extended rod flanked by a small and a large globular density, which likely correspond to the Smc hinge and head domains with or without ScpAB. In good agreement with data obtained for *Bs* Smc protein by rotary shadowing experiments, these images suggest that the two Smc coiled coils are mostly aligned side by side (Melby et al., 1998).

Juxtaposition of Smc Coiled Coils in Solution

We were concerned that the observed rod-like structure might arise during the harsh conditions used for EM sample preparation. Therefore, we probed the configuration of the Smc coiled coils under more physiological conditions by estimating the distance between symmetry-related positions on the two coiled coils in solution using fluorescence resonance energy transfer (FRET). We produced a *Bs* Smc fragment comprising the Smc hinge domain and a long stretch of coiled coil (~100 residues), designated as *Bs*SmcH-CC100 (Figure 1C). A single cysteine residue, Cys437, on the coiled coil was used for stochastic labeling with donor (Cy3) and acceptor (Cy5) dyes (Figure 1C). In order to discriminate the FRET pair (Cy3-Cy5 dimer) from any non-FRET pair (Cy3-Cy3 and Cy5-Cy5 dimers) in the sample, the single-molecule alternating-laser excitation FRET (ALEX-FRET) method was applied. The Cy3-Cy5 dimer species exhibited predominantly higher values of FRET efficiency, E, indicating that the two coiled coils are close to each other in most or all dimers of *Bs*SmcH-CC100 (Figure 1C). Based on the observed FRET efficiency, the distance between Cy3 and Cy5 was estimated to be around 44 Å (E = 0.86) or approximately twice the diameter of a coiled coil. Similar experiments performed on a related fragment of the MukB protein, which exists in an open V conformation, demonstrated the validity of our FRET approach (Figure 1D). Furthermore, low real-time fluctuations in single-molecule total internal reflection fluorescence (TIRF)-FRET suggest that the coiled coils of *Bs* Smc hinge fragments are mostly or always closely juxtaposed (Figure S1).

Structure of Juxtaposed Smc Coiled Coils

To elucidate the molecular basis for the alignment of Smc coiled coils, we determined the atomic structure of a fragment of *Pyrococcus furiosus* (*Pf*) Smc containing its hinge and a significant part of its coiled coil. After we screened several constructs with different lengths of coiled coil, crystals of a *Pf* Smc hinge domain with a 60-residue stretch of coiled coil, referred to as *Pf*SmcH-CC60, were obtained, and the phase problem was solved by molecular replacement using the structure of an isolated *Pf* Smc hinge (Table 1) (Griese and Hopfner, 2011). The asymmetric unit of the crystal contained two copies of the *Pf*SmcH-CC60 homodimer. As expected, the two hinge domains

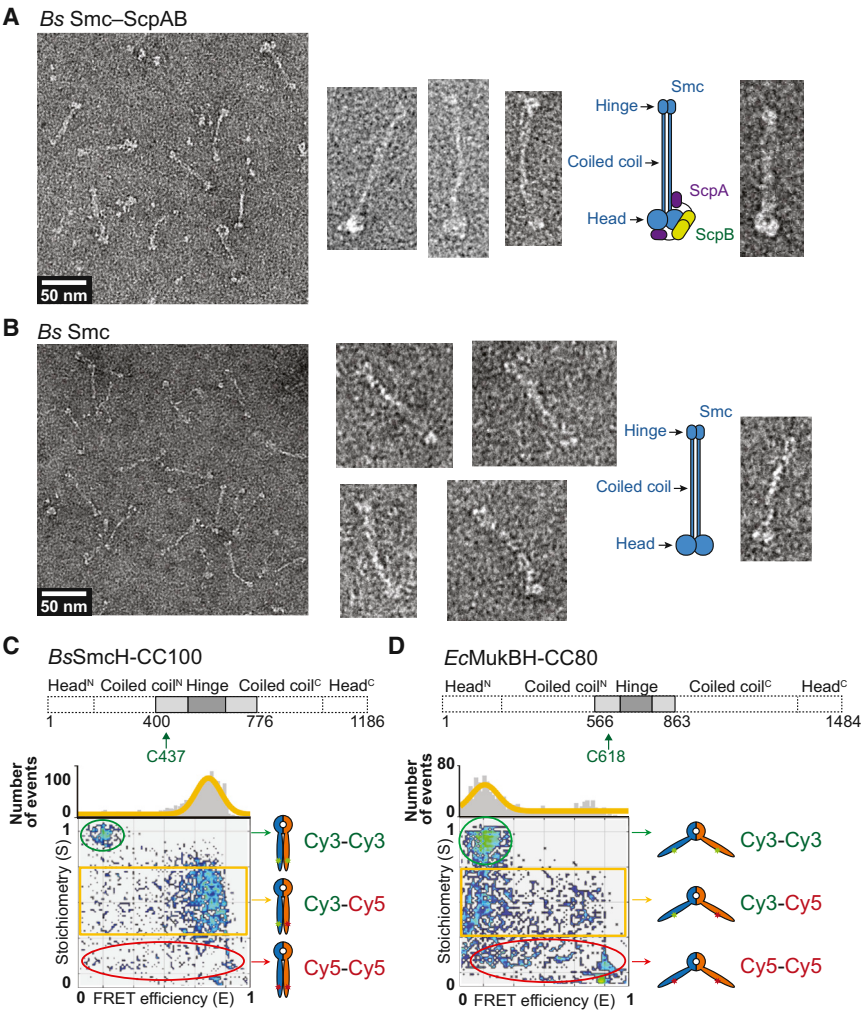

Figure 1. EM and FRET Analysis of Smc-ScpAB

(A) EM images of negatively stained *Bs* Smc-ScpAB. Selected objects are shown in high magnification (right).

(B) EM images of negatively stained *Bs* Smc protein.

(C) ALEX-FRET analysis of *Bs*SmcH-CC100 (schematic drawing of construct on top) stochastically labeled at C437 with Cy3 and Cy5. In the FRET efficiency versus stoichiometry graph, each dot denotes a single *Bs*SmcH-CC100 dimer. The green and red ellipses indicate dimers labeled by Cy3 or Cy5, respectively. Doubly labeled Cy3-*Bs*SmcH-CC100-Cy5 dimers (yellow box) exhibit mostly high FRET.

(D) Same as in (C) using *Ec*MukBH-CC80 labeled at C618.

See also Figure S1.

in the homodimer interact with each other at two identical interfaces to form a toroidal structure having a flat bottom and a central hole with the largest dimension of ~16 Å (Figure 2A; Figure S2A). The two coiled coils are aligned in parallel and are closely juxtaposed onto each other, thereby forming a rod-like overall structure. The coiled coils emanate from the Smc hinge perpendicular to the bottom surface of the toroid, reminiscent of tentacles radiating from the body of a jellyfish. This shape is a result of a sharp ~90° kink, governed by a single glycine residue (Gly507), at the junction between the N-terminal helix of the coiled coil and the following "rooting helix" α2, which interacts with a hydrophobic groove at the bottom of the toroid (Figure 2B). The presented architecture of the *Pf*SmcH-CC60 homodimer is in sharp contrast with the V-shaped organization of the *Tm* Smc hinge with short coiled coils (discussed later) and of the *Ec* MukB hinge with long coiled coils (Figure S2B) (Li et al., 2010).

Right below the bottom surface of the *Pf* Smc hinge, the two N-terminal coiled-coil helices of the homodimer pack against each other and engage in hydrophobic contacts (Figure 2C). In addition, ~80 Å (or ~50 residues) below the toroid, the two C-terminal coiled-coil helices are in contact with each other in a similar fashion (Figure 2C). This two-site interaction is found in both dimers of the asymmetric unit and appears to be responsible for holding the coiled coils together. Curiously, the two Smc coiled coils within a dimer display slightly distinct angles of attachment to the hinge, thus creating an asymmetric overall architecture (Figure 2A, right panel). This asymmetry might allow a more stable interaction to be formed at the coils/coils interface.

Smc-ScpAB Adopts a Rod-like Structure in *B. subtilis*

The coiled coils emanating from the Smc hinge adopt juxtaposed configurations in fragments of *Bs* and *Pf* Smc. However, multiple sequence alignments indicate that residues at the interfaces between the coiled coils in *Pf* Smc are not particularly well conserved (Figures 3A and 3B), raising the questions of whether this coils/coils interface is specific to archaeal Smc proteins or a general feature conserved through coevolution of pairs of residues. To test this, we probed the conformation of the coiled coils in endogenous holocomplexes of prokaryotic condensin using cysteine-specific crosslinking in living *Bs* cells. Based on the structure of *Pf*SmcH-CC60, we engineered single-cysteine residues into the predicted coils/coils interfaces of *Bs* Smc. As the coils/coils interface is located along the 2-fold symmetry axis, crosslinking of cysteines by the thiol reactive compound BMOE will occur between symmetry-related Cys residues, which are in close proximity (<8 Å). To determine crosslinking efficiencies, we made use of a C-terminal HaloTag fusion to Smc permitting in-gel fluorescence detection of Smc species (Bürmann et al., 2013). Based on sequence alignments and coiled-coil predictions, three residues in the N-terminal helix of the Smc coiled coil were chosen to be mutated to cysteine (D491C, M492C, and T495C) (Figure 3A). All three mutant Smc proteins are functional, as judged by growth on rich medium (data not shown) (Gruber et al., 2014). They displayed significant levels of Smc-Smc crosslinking after

Table 1. Data Collection and Structure Refinement Statistics

Data Collection	*Pf*SmcH-CC60	*Sc*Smc2H-CC110/ *Sc*Smc4H-CC110
Crystal	Native	selenomethionine substituted
X-ray source[a]	5C, PAL	BL17A, PF
Space group	$P2_12_12_1$	C2
Unit cell dimensions		
a, b, c (Å)	101.92, 116.88, 145.493	185.26, 49.71, 154.28
α, β, γ (°)	90, 90, 90	90, 92.52, 90
Wavelength (Å)	1.0000	0.9789
Resolution (Å)	50.0–3.5	50.0–2.9
R_{sym} (%)	9.3 (28.2)[b]	9.0 (33.8)[b]
I/σ(I)	26.2(5.3)	33.5(4.8)
Completeness (%)	89.5 (74.7)	90.2 (73.6)
Redundancy	5.6 (2.9)	4.4 (2.3)
Refinement		
Resolution (Å)	50.0–3.5	50.0–2.9
Number of reflections	20,012	49,139
R_{work}/R_{free} (%)	23.6/28.4	22.3/26.6
Root-mean-square deviations		
Bond (Å)/angle (°)	0.003/0.78	0.010/1.29
Average B values (Å^2)	47.08	84.58
Ramachandran plot (%)		
Most favored/favored	88.2/11.3	86.7/13.1
Generously allowed	0.2	0.2

[a]Beamline 5C at Pohang Accelerator Laboratory (PAL) and Beamline BL-17A at Photon Factory (PF).
[b]The numbers in parentheses are the statistics from the highest resolution shell.

incubation with BMOE, whereas a wild-type control showed little or no crosslinking (Figure 3C). Thus, the selected residues are located in close proximity of their symmetry mates, as predicted by the *Pf*SmcH-CC60 but not the *Tm* Smc hinge structure (Figure 3A). The alignment of sequences in the C-terminal helix of the Smc coiled coil is more ambiguous; therefore, several residues were mutated to cysteines in a region about 45–60 residues from the Smc hinge domain. Three cysteine residues (Q708C, K712C, and D716C) showed very little Smc-Smc crosslinking—likely because their side chains are too far apart or facing opposite sides of the coils/coils structure. In stark contrast, residues A715C and E722C supported robust crosslinking of Smc (Figure 3C). In summary, efficient crosslinking by specific cysteine residues demonstrates that the coiled coils emanating from the Smc hinge are held together by a defined interface in endogenous Smc-ScpAB complexes.

DNA Binding to the Hinge Facilitates Opening of Smc Arms

Given the fact that several SMC hinge domains display DNA binding affinity, we wondered whether the coiled-coil configuration would have any influence on the association of Smc with DNA. DNA binding activity of SMC hinges has been tentatively mapped to positively charged residues in the transition region between the hinge and the coiled coils in cohesin and Smc-ScpAB (Chiu et al., 2004; Hirano and Hirano, 2006). Accordingly, bound DNA might be located at the bottom surface of the hinge toroid (Figure 4A). Intriguingly, this area is obstructed in our *Pf* Smc structure by the presence of the aligned coiled coils, thus highlighting the possibility that a conformational change at the Smc hinge might control its association with DNA. Using fluorescence anisotropy measurements with short stretches of double-stranded DNA (dsDNA), we first confirmed that *Bs*SmcH-CC100 displays affinity for DNA in the submicromolar range (dissociation constant, K_D, ~0.1 μM) (Figure 4B). Consistent with the notion that the transition region is involved in DNA binding, we found that an isolated *Bs* Smc hinge (*Bs*SmcH) lacking this region fails to bind to DNA, whereas a slightly larger construct (*Bs*SmcH-CC8) binds DNA (K_D, ~0.2 μM) with an affinity similar to that of *Bs*SmcH-CC100. A Smc protein fragment harboring almost the entire Smc coiled coil attached to the hinge domain, designated as *Bs*SmcH-CC300, associated with DNA only poorly, indicating that the long coiled coils interfere with efficient DNA binding at the hinge, possibly because of stable occlusion of the DNA binding site (Figure 4B). Next, we wondered whether the coiled coils are still juxtaposed when *Bs*SmcH-CC100 is bound to DNA. To test this, we have purified *Bs*SmcH-CC100 harboring T495C or A715C for crosslinking of Smc coiled coils. Intriguingly, formation of crosslinked dimers of *Bs*SmcH-CC100 was strongly affected by the presence of DNA (Figure 4C). In contrast, DNA binding had no effect on the crosslinking of a pair of cysteines located at the hinge dimer interface (R558C/N634C) (Bürmann et al., 2013) (Figure 4C). Furthermore, a cysteine pair at the coils/hinge intersection (Q532C/S676C) displayed a modest but reproducible increase in intramolecular crosslinking in the presence of DNA (increased from 50% ± 1% to 60% ± 1%), implying that this cysteine pair might preferentially capture the more open conformation of the coiled coils (Figures 4C and S3D). We next repeated the crosslinking of A715C using bis-maleimide compounds having long linkers between the reactive groups (BM-PEG_3, ~30 Å; and BM-PEG_{11}, ~55 Å), which are able to capture more distant pairs of cysteines. BM-PEG_3 and BM-PEG_{11} exhibited robust crosslinking of A715C in the absence of DNA but failed to do so in the presence of DNA (Figure S3G), implying that the A715C residues are too distantly located to be bridged by either BM-PEG_3 or BM-PEG_{11} when *Bs*SmcH-CC100 is bound to DNA. As positive control for long-distance crosslinking, we created a pair of cysteines (R516C, S597C) located about 30 Å apart from each other on the Smc hinge domain. As expected, this cysteine pair was efficiently crosslinked by BM-PEG_{11}, but not by BM-PEG_3 or BMOE, regardless of the presence or absence of DNA (Figure S3G). Together, these findings strongly suggest that DNA binding stabilizes an open conformation of the coiled coils at the SMC hinge. Intriguingly, this immediately implies a molecular model of regulated DNA binding by Smc: ATP binding or hydrolysis at the Smc heads might facilitate opening of Smc arms and thus expose the DNA binding site at the hinge. To test this, we purified full-length *Bs* Smc and cysless Smc(A715C) and performed DNA binding and crosslinking studies in the absence

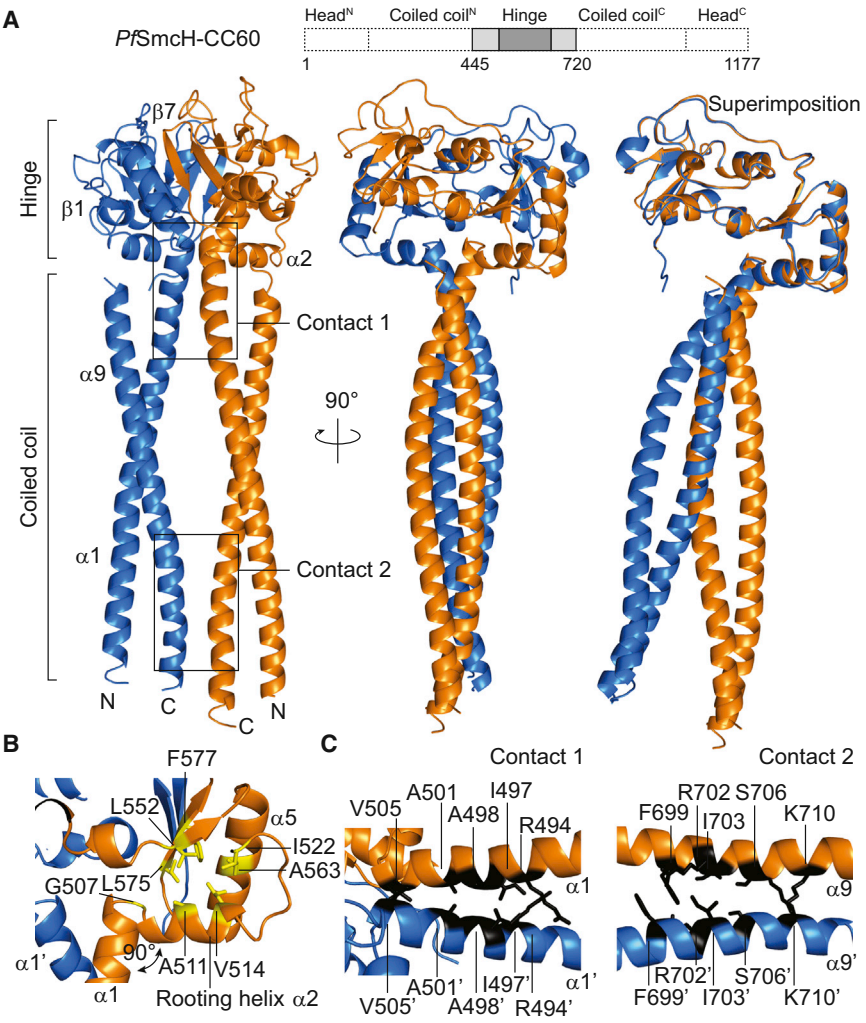

Figure 2. Structure of the *Pf* Smc Hinge with Long Coiled Coils

(A) Crystal structure of a dimer of *Pf*SmcH-CC60 shown in two perpendicular views (left and middle panels). Structural superimposition of the two monomers demonstrates slight asymmetry at the coils/hinge junction (right panel).

(B) Details of the coils/hinge interaction in *Pf* Smc. Conserved hydrophobic residues are displayed in stick representation in yellow. The arrow indicates a 90° kink at G507 between the coiled-coil helix, α1, and the rooting helix, α2.

(C) Structural view of the hinge-proximal (Contact 1, left panel) and hinge-distal coils/coils interface (Contact 2, right panel) in *Pf*SmcH-CC60.

See also Figure S2.

and presence of ATP. Without ATP, Smc imposed only a weak effect on the fluorescence anisotropy of DNA, indicating that the DNA binding site at the hinge is at least partly occluded in full-length Smc protein (Figure 4D). In the presence of ATP, however, the anisotropy response was substantial, producing an affinity (K_D, ~0.1 μM) similar to that of Smc hinge fragments. Exclusively under these conditions (i.e., with DNA and ATP), crosslinking of Smc arms at A715C was strongly reduced (Figure 4E). A hydrolysis-defective Smc mutant (E1118Q) displayed normal Smc arm opening, whereas a mutant blocked in Smc head engagement (S1090R) was locked in the rod-like state, suggesting that ATP-dependent head engagement drives dissolution of Smc rods (Figure 4E). Thus, Smc arms undergo an extended structural transition, which is cooperatively promoted by binding of DNA to the Smc hinge and ATP to the head domains.

Artificial Opening of Smc Arms Is Detrimental

If the observed conformational change was physiologically relevant, then locking Smc-ScpAB in the open or closed configuration should jeopardize its functionality. Because of the extensive nature of the coils/coils interface and the rigid connection to the hinge, mutations in single residues are unlikely to have significant impact on the overall architecture. Thus, we decided to replace parts of the *Bs* Smc protein with homologous protein fragments, which might intrinsically bear higher propensity for one or the other conformation. The *Tm* hinge was chosen because it adopts an open, V-shaped organization in protein crystals. With the help of available structural information, a chimeric protein was constructed by splicing together N- and C-terminal sequences of *Bs* Smc with the central part of *Tm* Smc comprising its hinge domain and short stretches of the adjacent coiled coil (Figure 5A). The resulting *Bs*Smc*Tm*H protein was expressed from the endogenous locus in *Bs*. It accumulated at normal levels in vivo and efficiently formed Smc dimers according to crosslinking analysis, implying that protein folding was mostly unperturbed (data not shown). However, its functionality was severely compromised, as judged by colony formation assays (Figure 5A) (Gruber et al., 2014). To identify the underlying cause for this loss of function in *Bs*Smc*Tm*H, we mutagenized its *Tm* hinge moiety and isolated suppressor mutations that enabled normal growth on rich medium (Figure S4A). Most suppressor mutations mapped in the vicinity of the connection between the *Tm* Smc hinge and the adjacent coils, suggesting that these mutations might indeed provide increased structural flexibility at the coils/hinge interface (Figure 5B). Alternatively, these mutations could affect DNA binding to the *Tm* hinge. Although the *Tm* Smc hinge bound DNA in a more salt-sensitive manner than the *Bs* Smc hinge, the suppressor mutation S535N had no effect on the DNA binding of a chimeric Smc hinge fragment with long coiled coils (Figure S4B). Thus, defects in DNA binding at the *Tm* hinge are an unlikely explanation for the loss of functionality in *Bs*Smc*Tm*H. To measure the juxtapositioning of Smc arms in chimeric Smc proteins, we next fused a C-terminal HaloTag to *Bs*Smc*Tm*H and introduced the cysteine residue

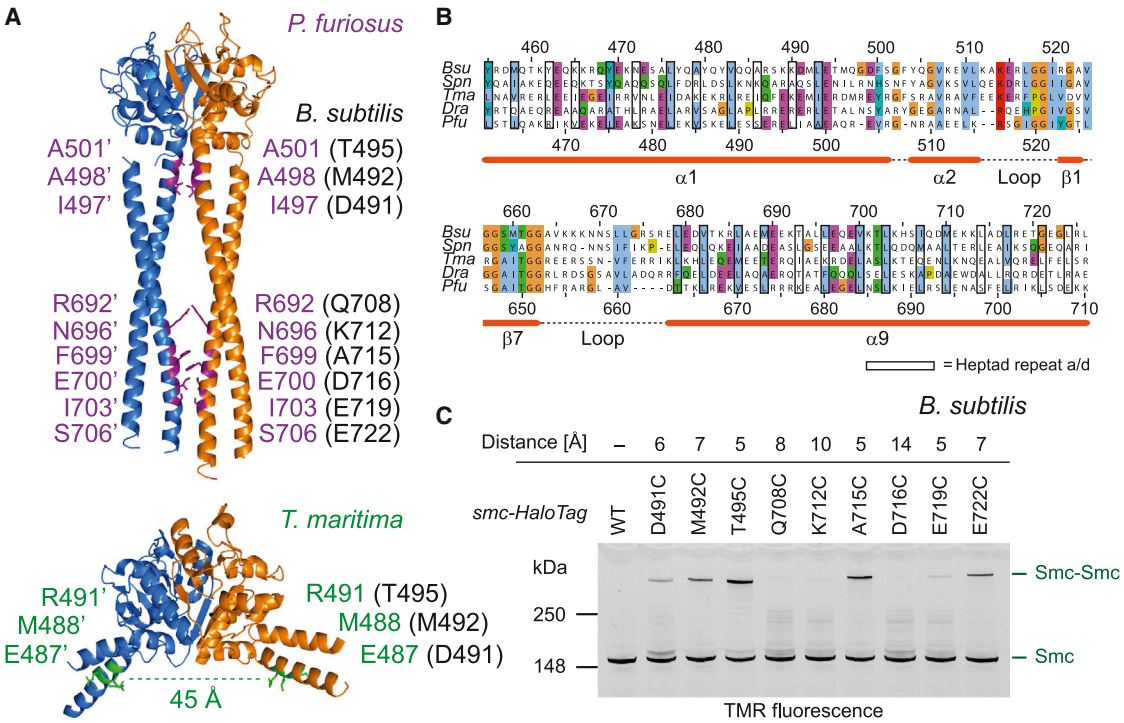

Figure 3. Juxtapositioning of the Smc Coiled Coils in *Bs* Smc-ScpAB

(A) Map of residues located at the coils/coils interface of *Pf*SmcH-CC60 (top). Equivalent positions in *Bs* Smc were identified based on the sequence alignment shown in (B). In the *Tm* Smc hinge structure (PDB ID: 1GXL), these residues are distantly located from their symmetry mates (bottom panel). Labels for amino acids in *Pf*, *Tm*, and *Bs* Smc are shown in purple, green, and black, respectively.

(B) Alignment of the N- and C-terminal coils/hinge junctions (top and bottom panels, respectively) of four bacterial and one archaeal Smc protein sequence. (*Bsu*, *Bs*; *Dra*, *D. radiodurans*; *Pfu*, *Pf*; *Spn*, *S. pneumoniae*; *Tma*, *Tm*) Secondary structure elements are based on the structure of *Pf*SmcH-CC60.

(C) In vivo crosslinking of cysteine mutants of *Bs* Smc-HaloTag with BMOE. Distances between symmetry-related Cys residues in *Bs* Smc were estimated according to the *Pf*SmcH-CC60 structure. Cells were grown in Luria-Bertani medium. Strains: BSG1711, BSG1760–1765, and BSG1821–1823.

A715C for crosslinking. Crucially, the arms of the nonfunctional *Bs*Smc*Tm*H protein were only poorly crosslinked by BMOE, suggesting that the *Tm* hinge domain in *Bs*Smc*Tm*H promotes a more open coiled-coil arrangement, as suggested by its crystal structure (Figure 5C). Notably, the suppressed version, *Bs*Smc*Tm*H(S535N), displayed wild-type levels of Smc arm crosslinking. Thus, the ability to efficiently adopt the rod-shaped conformation appears crucial for Smc function. In combination with the observation that DNA binding stabilizes the open form, this finding strongly supports the notion that both open and closed conformations are crucially important for condensin function. We propose that transitions from rod-like to ring-like states and vice versa are essential for the biochemical action of Smc-ScpAB.

Structure of a Yeast Smc2-4 Hinge Heterodimer with Long Coiled Coils

Eukaryotic condensin has been observed as a rod-like structure by EM, suggesting that the architecture of the coils/hinge connection might be conserved between pro- and eukaryotic SMC complexes. The structure of a mouse Smc2-4 hinge heterodimer has recently been solved (Griese et al., 2010). However, because of the lack of coiled coils, no insight into their arrangement with respect to the hinge was gained. To address this, we generated a number of yeast Smc2 and Smc4 constructs containing the hinge domain and long stretches of coiled coil. Of these, Smc2 (residues 396–792) and Smc4 (residues 555–951), referred to as *Sc*Smc2H-CC110 and *Sc*Smc4H-CC110, respectively, were crystallized as a heterodimeric complex (Figure 6A). The coiled-coil stretches in these proteins correspond to about 150-Å-long α helices or approximately one third of the entire length of the Smc2 and Smc4 coiled coils.

The hinge domains of *Sc*Smc2H-CC110 and *Sc*Smc4H-CC110 together form a toroid structure having a central hole similar to the counterparts in Smc-ScpAB and cohesin (Figure 6B) (Haering et al., 2002; Kurze et al., 2011). Strikingly, however, the segments connected to the coiled coils are very different between the two subunits in their secondary structures and arrangement (Figures 6C and 6D). Opposite orientations of the coiled coils with regard to their hinge domain make them run in parallel upon heterodimerization of Smc2 and Smc4 to produce a highly asymmetric, folded rod-like overall structure.

The coiled coil of *Sc*Smc4H-CC110 is entirely visible and extends out by about 150 Å. In case of *Sc*Smc2H-CC110, about half of its coiled coil is visible in the electron density map (Figure 6A). The end of the Smc4 coiled coil is involved in crystal packing, whereas that of the Smc2 coiled coil is not.

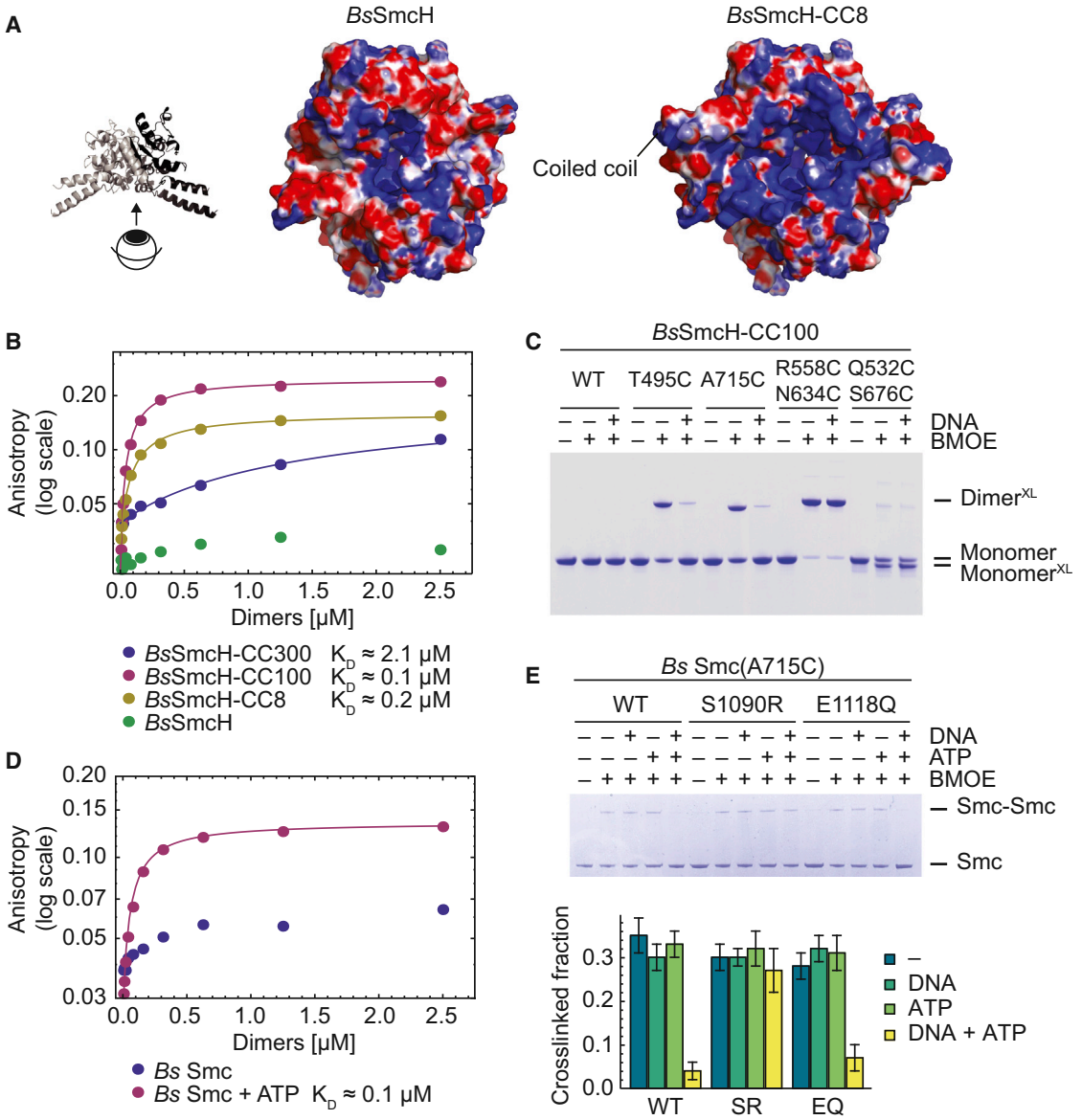

Figure 4. Structural Changes at the Coils/Hinge Junction upon DNA and ATP Binding

(A) Bottom view of electrostatic surface potential maps of *Bs* Smc hinge models (Kurze et al., 2011) based on the *Tm* Smc hinge structure (PDB ID: 1GXL). Left: isolated *Bs* Smc hinge. Right: hinge with short coiled coils.

(B) DNA binding of *Bs* Smc fragments measured by fluorescence anisotropy using fluorescein-labeled DNA (40 bp).

(C) Crosslinking of cysteine-bearing variants of *Bs*SmcH-CC100 with and without DNA. XL denotes species crosslinked by BMOE. WT, wild-type.

(D) DNA binding of *Bs* Smc in the presence and absence of ATP measured by anisotropy using fluorescein-labeled DNA (40 bp).

(E) Crosslinking of *Bs* Smc(A715C) variants with and without mutations in the ABC signature and Walker B motif (S1090R [SR] and E1118Q [EQ], respectively). The four endogenous cysteines have been replaced by serines. Quantification of crosslinking efficiency is based on three independent replicates. Data are represented as mean ± SEM.

See also Figure S3.

Alignment of Smc2-4 Coiled Coils in the Condensin Holocomplex

Does the crystal structure faithfully reflect a conformation adopted by condensin holocomplexes isolated from yeast? To test this, we probed the complex by site-specific crosslinking with BMOE. We identified pairs of residues at the coils/coils interface of Smc2 and Smc4 that are in close proximity in the crystal structure and mutated them to cysteines (Figure 6E). For some cysteine combinations, the endogenous Cys494 in Smc2 was replaced by serine to prevent interference with the assay. Cysteine mutations were combined with a HaloTag on Smc2 and a Pk_6 tag on Smc4 and introduced into the respective endogenous genetic

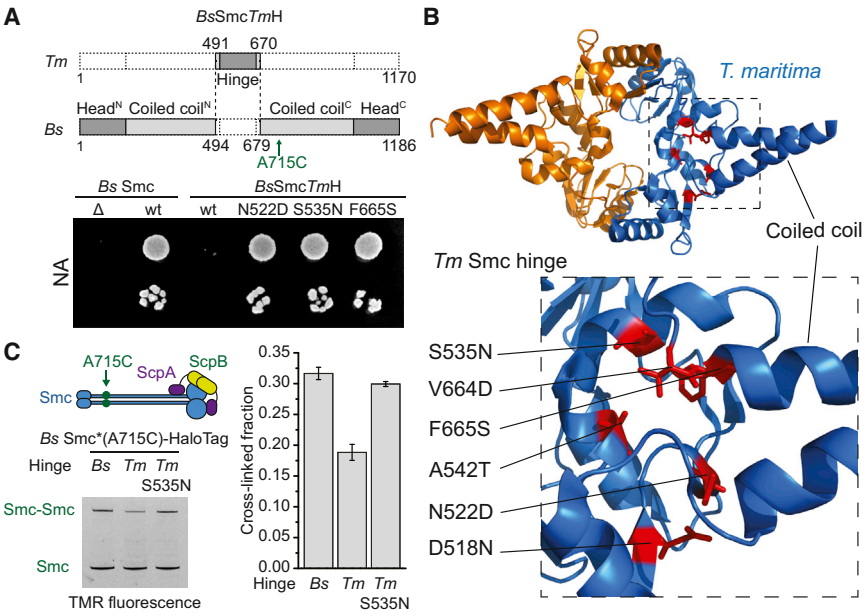

Figure 5. Artificial Opening of Smc Arms at the Hinge Is Detrimental in *B. subtilis*

(A) Schematic drawing of the *Bs*Smc*Tm*H construct (top). Colony formation assay of strains of *Bs* encoding variants of *Bs* Smc or *Bs*Smc*Tm*H as the single source of Smc protein on nutrient-rich medium. Strains: BSG1001, BSG1007, BSG1363, BSG1365, BSG1368, and BSG1970.

(B) Mapping of suppressor mutations onto the *Tm* Smc hinge structure (PDB ID: 1GXL). Residues altered in *Bs*Smc*Tm*H suppressor mutants are highlighted in red as sticks.

(C) In vivo cysteine crosslinking of *Bs* Smc(A715C), *Bs*Smc*Tm*H(A715C) and its functional variant harboring the S535N mutation. All four endogenous cysteines have been replaced by serines. The graph shows means and SD from triplicate reactions. Cells were grown in SMG medium. Strains: BSG1921, BSG1932, and BSG1934.

See also Figure S4.

loci of a haploid yeast strain. The modified genes were expressed as the sole source of *SMC2* and *SMC4* and supported viability, indicating that condensin remained functional. We then used antibodies against the Pk epitopes on Smc4 to immunoprecipitate holocomplexes from asynchronous cultures. Immobilized complexes were treated with the crosslinker BMOE and conjugated to the HaloTag-tetramethylrhodamine (TMR) substrate. Subsequently, crosslinked species of Smc2-HaloTag were detected by in-gel fluorescence (Figure 6F). When wild-type complexes were treated with BMOE, crosslinking of Smc2 to Smc4 was hardly detectable. Similarly, only insubstantial crosslinking was observed with cysteine pairs when their thiol group distance exceeded the ~8 Å linker length of BMOE. In contrast, introduction of more closely positioned pairs of cysteines promoted robust crosslinking of Smc2 and Smc4 (Figure 6F). These data strongly suggest that the conformations of the coiled coils observed by X-ray crystallography are adopted by native condensin holocomplexes.

Structural Basis and Conservation of the Parallel Orientations of the Smc2-4 Coiled Coils

Quite extensive hydrophobic interactions are found at the coils/hinge interface in condensin, a feature that is much less pronounced or lacking in prokaryotic condensin. For description, we designate the N-terminal α-helix of the Smc2 coiled coil as N-αH^{2CC} and the C-terminal α-helix as C-αH^{2CC}; likewise, we designate those of the Smc4 coiled coil as N-αH^{4CC} and C-αH^{4CC}. In the case of the Smc4 coiled coil, N-αH^{4CC} is longer than C-αH^{4CC}, and the last part of N-αH^{4CC} (residues 665–682) does not interact with C-αH^{4CC} but with the Smc4 hinge domain. This α-helical segment of Smc4—which, in analogy to the *Pf* structure, we call "rooting α-helix"—has at least three hydrophobic residues (Val672, Leu676, and Leu679) that interact with a hydrophobic groove on the Smc4 hinge domain (Figure 6C). These interactions are quite extensive and appear to be responsible for fixing the position and the orientation of the Smc4 coiled coil. Notably, the key hydrophobic residues involved in the Smc4 hinge/coiled coil interaction are conserved throughout eukaryotic condensins. Consistent with this notion, we found that mutation of hydrophobic residues L676 or L731—located at the Smc4 hinge/coil interface—to aspartate rendered the protein nonfunctional in yeast (Figures S5A–S5F). The Smc2 coiled coil associates with the hinge heterodimer at a hydrophobic interface involving Leu676, Leu677, and Ile680 at the beginning of C-αH^{2CC} and Leu507, Phe531, Ile533, Leu552, and Phe553 on the Smc2 hinge domain (Figure 6D). All these residues are also well conserved. However, single mutations in the residues in C-αH^{2CC} did not result in any obvious growth defects (Figures S5G–S5I). Nevertheless, the high level of sequence conservation suggests that the observed conformations of the Smc2 and Smc4 coiled coils relative to the hinge domains are likely a general feature of condensin in eukaryotes.

In addition to the coils/hinge interactions, also coils/coils interactions are found. The Smc2 coiled coil is in contact with the Smc4 coiled coil at one site via three exposed hydrophilic interactions and one ring-to-ring stacking interaction (Figure S5K). The hydrophilic interactions are solvent exposed, and the contacting helices are not tightly packed against each other, unlike those observed in the *Pf*SmcH-CC60 structure (compare Figures 2C and S5K). Therefore, these coils/coils interactions appear to be a result, rather than a cause, of the juxtaposition of the coiled coils, although they might reinforce the parallel orientations of the coiled coils.

The *Sc*Smc2H-CC110/*Sc*Smc4H-CC110 complex binds dsDNA with high affinity (K_D ~50 nM; measured by fluorescence anisotropy). However, the crosslinking of two pairs of cysteines [Smc2(K487C)-Smc4(E876C) and Smc2(K495C)-Smc4(E866C)] at its coils/coils interface is unaffected by the presence of short

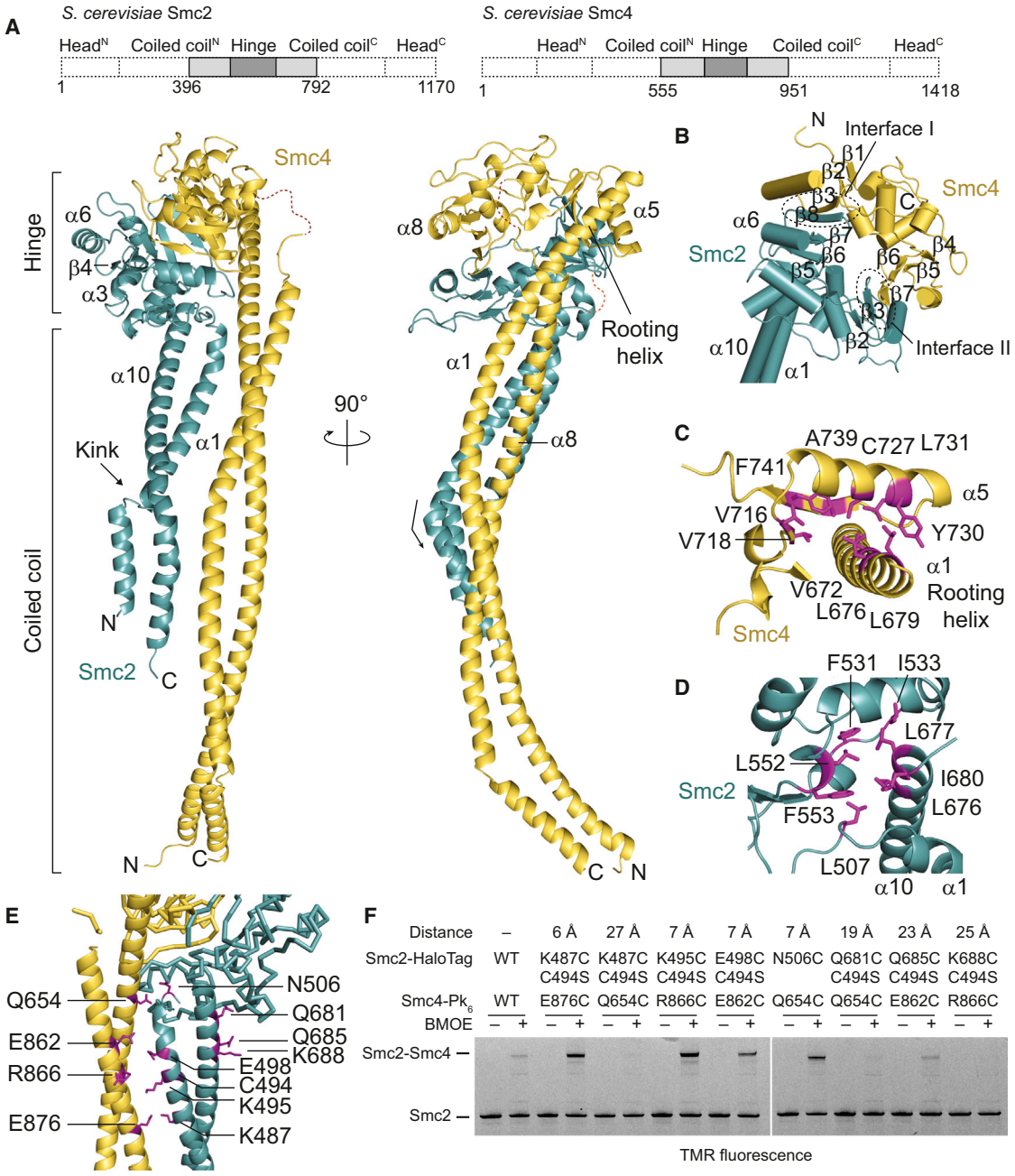

Figure 6. Structure of the Yeast Smc2-4 Hinge with Long Coiled Coils

(A) Crystal structure of a heterodimer of *Sc*Smc2H-CC110 and *Sc*Smc4H-CC110 proteins in cartoon representation in green and yellow, respectively, in two perpendicular views. The dotted lines indicate disordered segments in Smc2 and Smc4.

(B) The hinge domain toroid and the two interfaces between Smc2 and Smc4, each composed of two short β strands. The Smc4 coiled coil is omitted for clarity.

(C) Details of the Smc4 coils/hinge interface. Residues at the interface are shown in stick representation in pink.

(D) Smc2 coils/hinge interface.

(E) Coils/coils interface. Residues at the Smc2-4 coils/coils interface mutated to cysteine are indicated in stick representation in pink.

(F) Cysteine crosslinking of Smc2 and Smc4 coiled coils in holocomplexes of yeast condensin. Distances between pairs of Smc2 and Smc4 cysteine residues are predicted based on the crystal structure. Yeast condensin was immunoprecipitated with antibodies against the Pk_6 epitope tag on Smc4 and crosslinked with BMOE. Smc2-HaloTag protein was fluorescently labeled and analyzed by in-gel detection. Strains: YSG81, YSG99–102, YSG158, and YSG192–194.

See also Figure S5.

DNA molecules (40 base pairs [bp]) (data not shown). A surface potential map of the Smc2-4 structure features a prominently positively charged area on top of the Smc2-4 hinge (Figure S6E), suggesting that initial DNA contact might occur at the top hinge surface in condensin. Possibly, additional elements such as ATP binding to the Smc2-4 heads, non-SMC subunits, loading factors, or nucleosomes might control any binding of DNA to the bottom hinge surface and/or opening of condensin SMC arms. To address the first two possibilities, we purified endogenous yeast condensin from exponentially growing or mitotically arrested populations of cells harboring Smc2(K495C) and Smc4(E866C) mutations by immunoprecipitation or affinity tag purification. Purified fractions of yeast condensin were then incubated with BMOE crosslinker in the presence or absence of ATP and short DNA. However, no significant differences in crosslinking were detected under the various conditions (data not shown). Thus, these attempts failed to provide evidence for the opening of SMC arms in yeast condensin in vitro.

Open or Closed SMC Arms at the Cohesin Hinge?

Several EM studies depict cohesin and MukBEF in wide open conformations. In case of the latter, the open architecture is further supported by crystal structures of three isolated hinge fragments, all displaying diametrically opposed coiled coils (Ku et al., 2010; Li et al., 2010; Vos et al., 2013). Conceivably, cohesin and MukBEF might be fundamentally different in their structure from both condensin and Smc-ScpAB. Alternatively, all SMC complexes might require closed and open conformations during the course of action but might have distinct intrinsic preferences for these arrangements. To our surprise, we found that the coils/hinge junction in cohesin bears a strong resemblance to condensin. A crystal structure of the cohesin Smc1-3 hinge heterodimer was reported previously (Kurze et al., 2011). It contains a very short Smc3 coiled coil and a short α-helix of Smc1 that corresponds to the rooting α-helix of Smc4. Structural comparison with *Sc*Smc2H-CC110/*Sc*Smc4H-CC110 shows that the short Smc3 coiled coil is oriented similarly as the Smc2 coiled coil and that the short α-helix of Smc1 points in the same direction as the rooting α-helix of Smc4 (Figure 7A). Furthermore, most hydrophobic residues important for the coils/hinge interaction in the Smc2-4 heterodimer are conserved in Smc1 and Smc3 proteins. To address whether cohesin Smc1-3 complexes may indeed be able to adopt a rod shape, we generated a *Sc*Smc1H-CC100/*Sc*Smc3H-CC50 dimer and analyzed its structure using small-angle X-ray scattering (SAXS), a robust technique for characterization of macromolecular conformations in solution (Hura et al., 2009; Rambo and Tainer, 2010, 2013). As proof of principle, we initially performed SAXS analysis on *Pf*SmcH-CC60 and an *Ec* MukB hinge fragment with long coiled coils, designated as *Ec*MukBH-CC80. For both proteins, molecular envelopes fitted accurately to the rod-shaped or open V-shaped structures obtained by X-ray crystallography (Figures 7B–7D; Figure S6C; Table S3). These findings demonstrate that the coils/hinge junctions have a defined structure in solution as previously indicated by FRET analysis (Figures 1C and 1D). In addition, these experiments confirm the validity and suitability of SAXS for the study of SMC coils/hinge organization. Next, we analyzed the architecture of the *Sc*Smc1H-CC100/*Sc*Smc3H-CC50 dimer by SAXS. Remarkably, the SAXS envelopes derived for the cohesin fragment were clearly too short to accommodate an open V-shaped dimer as seen for *Ec*MukBH-CC80 but were similar in size and shape to the condensin structure (Figures 7B–7D; Figure S6C), suggesting that Smc1-3 proteins fold into rods in solution. Two additional pieces of evidence support this surprising notion. First, a comprehensive lysine proximity map of purified human cohesin—based on the identification of crosslinked peptides by mass spectrometry by the Jan-Michael Peters laboratory—revealed 19 juxtaposed pairs of Smc1 and Smc3 coiled-coil residues (out of a total of 51 on cohesin) (Huis in 't Veld et al., 2014). Almost all these chemical crosslinks occurred between residues with similar position (plus or minus ten amino acids) along the length of the Smc1 and Smc3 coiled coils, being consistent with a well-defined, physical association between the two coiled coils (J.-M. Peters, personal communication). Second, we found that the affinity of the human cohesin hinge for DNA is reduced about 2-fold when 100 amino acids long coiled coils are attached to the Smc1 and Smc3 hinge domains, indicating that the DNA binding site at the cohesin hinge might at least be partially occluded (Figure S6D). Although further studies are clearly necessary, these initial observations provide an indication that all SMC complexes—with the possible exception of MukBEF—might at least transiently adopt a rod-like structure with juxtaposed coiled coils. Intriguingly, cohesin, condensin, and Smc hinge domains, but not the MukB hinge (Ku et al., 2010) (data not shown), display decent affinity for DNA, highlighting the possibility of a conserved functional connection between hinge architecture and regulated association with DNA.

DISCUSSION

Little information is available on the arrangement of the two long coiled coils in SMC-kleisin complexes in vivo. Here, we start to fill this void by solving high-resolution X-ray structures of prokaryotic Smc-ScpAB and eukaryotic condensin and by performing subsequent biochemical and genetic characterization. We identify close juxtapositioning of SMC coiled coils at the hinge domain as a predominant architectural theme in SMC complexes and establish a functional link between hinge structure and DNA association.

Rod Formation in Prokaryotic Smc-ScpAB and Eukaryotic Condensin

Our work demonstrates how the long coiled coils in *Bs* Smc-ScpAB and yeast condensin are attached to their hinge domain dimers. The respective parts of these complexes share two striking structural features: the toroid-like hinge formed by homo- versus heterotypic interaction of two hinge domains and a four-helix bundle built by the intimate alignment of two SMC coiled coils. The most pronounced difference between the two structures, however, is the orientation of the coiled coils with respect to the hinge-domain toroid. Whereas the two coiled coils in the prokaryotic Smc hinge are virtually symmetric and perpendicular to the hinge toroid, those in the eukaryotic hinge are highly asymmetric and roughly parallel to the plane of the bottom surface of the hinge toroid (Figure S6A). The difference possibly reflects

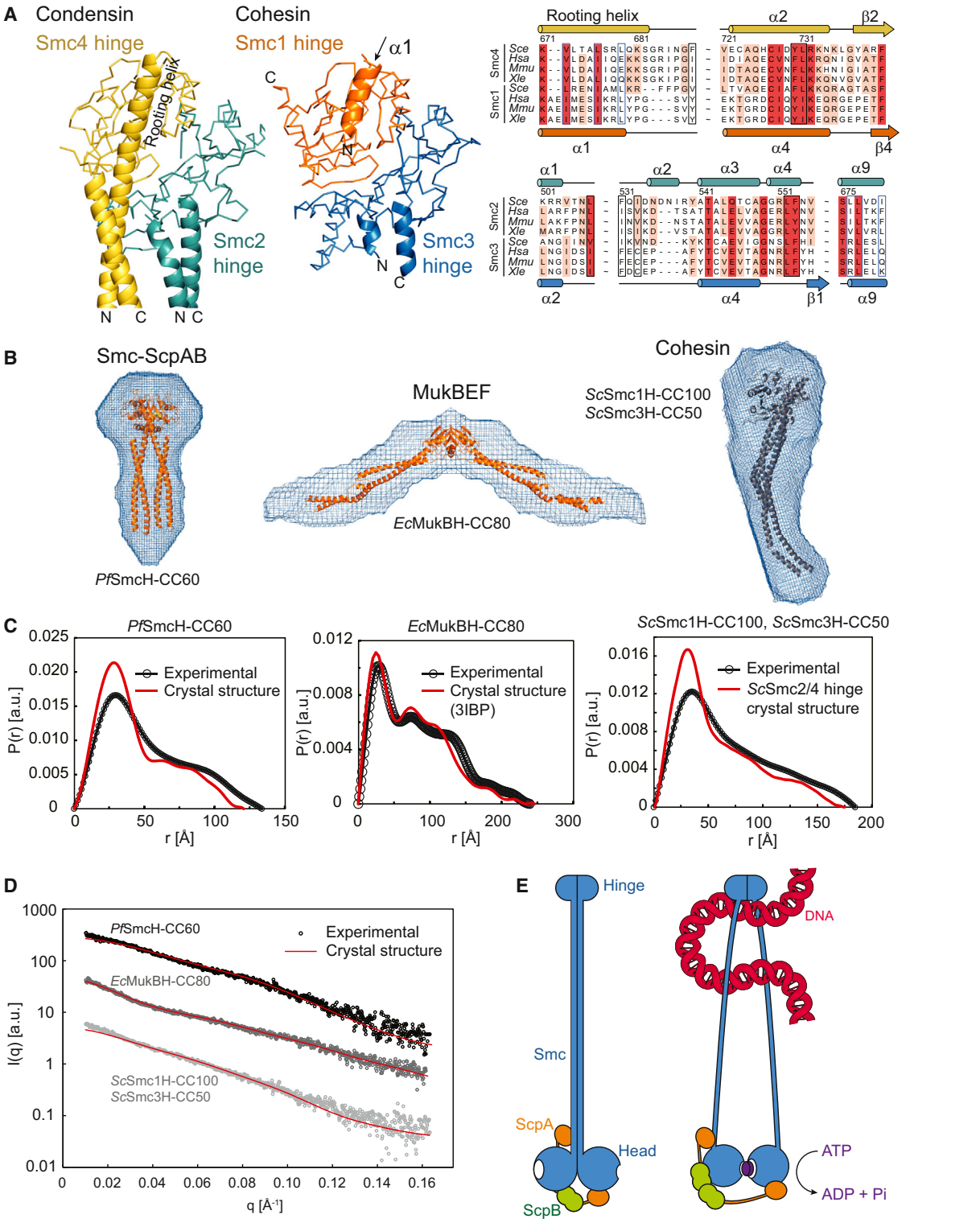

Figure 7. Organization of the Coils/Hinge Junction in Different SMC Complexes

(A) Side-by-side structural views of condensin hinge domains (*Sc*Smc2H-CC110/*Sc*Smc4H-CC110) (left) and cohesin hinge domains (PDB ID: 2WD5) (middle) reveals similarities in the attachment of coiled-coil helices onto the SMC hinge. Alignment of cohesin and condensin sequences at the coils/hinge junctions (right). (B) SAXS envelopes for dimers of SMC hinge fragments with attached coiled coils of variable length: *Pf*SmcH-CC60, *Ec*MukBH-CC80, *Sc*Smc1H-CC100/*Sc*Smc3H-CC50.

(legend continued on next page)

the homo- versus heterodimerization of these SMC proteins. The rooting α-helix of the yeast Smc4 hinge corresponds to α2 of the *Pf* Smc hinge. It can form a single straight α-helix with the preceding N-terminal Smc4 coiled-coil helix, as the Smc2 coiled coil keeps the required space free by adopting a different orientation. In contrast, α2 and the N-terminal coiled coil helix in the *Pf* Smc hinge cannot form a single continuous helix, because two such helices on the homodimer would inevitably clash with each other because of the molecular symmetry (Figure S6B). The ~90° bending at the junction between the two helices avoids this scenario and, instead, allows the coiled coils to stretch out in an I shape from the hinge toroid and juxtapose onto each other. Apparently, as Smc2 diverged from prokaryotic Smc, it changed the orientation of its coiled coil drastically through a unique interaction between C-αH^{2CC} and the hinge domain. It is important that, while eukaryotic SMC proteins broke the symmetry at the hinge, they retained the parallel and juxtaposed organization of the coiled coils, thus underscoring its functional importance.

The folded structure of prokaryotic Smc-ScpAB and eukaryotic condensins may be a way to limit the total number of entrapped DNA molecules within their circumference and/or to ensure that condensin would be occupied by selected DNA fibers only at defined moments in its catalytic cycle.

A Rod-to-Ring Transition in Smc-ScpAB—Regulating DNA Binding and Making a First Step toward Ring Opening?

Juxtapositioning of Smc coiled coils at the hinge is likely not a permanent feature. Rather, Smc-ScpAB complexes undergo marked transitions at the hinge between the folded rod and a more open ring-like configuration. The latter conformation is promoted by ATP binding to Smc heads and DNA binding to the hinge, whereas the former seems to be an intrinsically more favorable resting state. How could SMC proteins convert from one state to the other? EM images suggest that Smc arms are closely aligned along their entire length (Figure 1). During the ATP hydrolysis cycle, however, the head-proximal coiled coil might transiently become fixed in a conformation that is incompatible with coiled-coil juxtapositioning in this region (Haering et al., 2004). This, in turn, might promote the progression of coiled-coil disengagement up to the hinge, as seen in our BMOE crosslinking experiments (Figure 4E). We propose that the rod-like and ring-like configurations of Smc-ScpAB resemble, in structural and functional terms, the inward- and outward-facing conformations of the related ABC transmembrane transporters. In ABC transporters, the transitions between these conformations are controlled by the occupancy of the substrate binding pocket, thus ensuring unidirectional transport of substrates across membranes via a defined series of conformational states (Oldham et al., 2008). Our results give an indication as to how binding of the substrate molecule, DNA, might be restricted to the more open conformation of Smc by exposure of an otherwise occluded interface for DNA at the hinge. The hinge might thus serve as a sensor for DNA that links Smc arm architecture to the presence of DNA. Once DNA is bound to the hinge, it might stimulate hydrolysis of ATP by Smc (Hirano and Hirano, 2006) by simply promoting head engagement or through another long-range conformational change.

The location of the DNA binding site on the inner surface of the Smc hinge also has strong implications on how DNA might initially get in contact with Smc-ScpAB rings. Circular DNA molecules, such as bacterial chromosomes, need to form loops within the circumference of a SMC-kleisin ring so that DNA can fully engage with the binding site at the inner face of the hinge (Figure 7E). It will be exciting to determine the fate of the hinge-bound stretch of DNA—and the proposed DNA loop—upon completion of the loading reaction. Reformation of Smc rods will likely require the prior eviction of DNA from between Smc arms. We can think of two possible scenarios: (1) passage of DNA toward the head domains or (2) exit of DNA from the Smc-ScpA ring through a transiently opened hinge. The former could be related to processive extrusion of DNA loops from the Smc-ScpAB ring (Alipour and Marko, 2012; Nasmyth 2001), whereas the latter could create a topological interaction between circular DNA and Smc-ScpAB, as seen with cohesin and condensin, starting from a DNA loop. In this scenario, opening of the Smc-ScpAB ring might occur in two steps: by initial disengagement of Smc coiled coils and by subsequent hinge opening, possibly triggered by ATP hydrolysis.

Intriguingly, causative mutations in genes for cohesin subunits in Cornelia de Lange syndrome (CdLS) patients are mainly found in Smc1 and Smc3 coiled-coil sequences. In addition, several mutations that are located near the coils/hinge transition have been shown to increase DNA binding by Smc1-3 hinge heterodimers (Revenkova et al., 2009). Our data raise the exciting possibility that CdLS cohesin might be defective in SMC rod formation and, thus, display increased or misregulated association with DNA. Accordingly, cohesin in CdLS patients might have lost tight coordination between DNA binding at the hinge and the ATPase activity located at the SMC heads.

SMC proteins share their unusual architecture with Rad50, which uses a "zinc hook" rather than an SMC hinge domain for dimerization. Rad50 associates with Nbs1 and the nuclease Mre11 to form the MRN complex that is crucially important for efficient repair of DNA double-strand breaks and other DNA lesions (Williams et al., 2007). Simple binding of DNA to isolated Rad50 proteins has been suggested to convert ring-like dimers into straight rod-shaped structures (Moreno-Herrero et al., 2005). Thus, transitions between rod-like and ring-like states

(C) SAXS. Measured and calculated distance-distribution functions for different SMC hinge fragments (shown in B). a.u., arbitrary units.
(D) Experimental SAXS data for *Pf*SmcH-CC60, *Ec*MukBH-CC80, and *Sc*Smc1H-CC100/*Sc*Smc3H-CC50 and theoretical scattering curves calculated from the crystal structures of *Pf*SmcH-CC60, *Ec*MukBH-CC80, and *Sc*Smc2H-CC110/*Sc*Smc4H-CC110, respectively. For clarity, the curves are displayed with a y axis offset. Discrepancies (χ^2) between the experimental and theoretical curves are *Pf*SmcH-CC60 = 9.03, *Ec*MukBH-CC80 = 4.22, and *Sc*Smc1H-CC100/*Sc*Smc3H-CC100 = 9.08. Relevant scattering derived parameters are shown in Table S3.
(E) Tentative model for a large structural transition in Smc-ScpAB upon binding to DNA.
See also Figure S6 and Table S3.

might be a conserved, albeit differently regulated, feature of all SMC-like proteins.

EXPERIMENTAL PROCEDURES

Detailed methods can be found in the Supplemental Experimental Procedures.

Crystallization, X-Ray Data Collection, and Structure Determination

The *Pf*SmcH-CC60 crystals grew from a precipitant solution containing 1 M sodium citrate, 0.1 M CHES (pH 9.5), and 8% glycerol; and the *Sc*Smc2H-CC110/*Sc*Smc4H-CC110 crystals grew from a solution of 16% polyethylene glycol 300, 0.1 M Na/K phosphate (pH 6.0), 8% glycerol, and 10 mM dithiothreitol (DTT). The structure of *Pf*SmcH-CC60 was determined by molecular replacement using the structure of the coiled-coil-less *Pf* Smc hinge (Protein Data Bank [PDB] entry: 3NWC) as a search model. The *Sc*Smc2H-CC110/*Sc*Smc4H-CC110 structure was solved by the single isormorphous replacement with anomalous scattering method (Table 1).

SAXS Analysis

BL45XU of SPring-8 (Hyogo, Japan), 4C SAXS II beamline of Pohang Light Source II (Pohang, Korea) and a BioSAXS-1000 system (Rigaku) were used to collect SAXS intensity data. The data were processed and analyzed using the software applications embedded in the ATSAS package.

ALEX-FRET and TIRF-FRET Analyses

*Bs*SmcH-CC100 was labeled with Cy3- and Cy5-maleimide (GE Healthcare). The LABVIEW software (National Instruments) was used to select fluorescent bursts induced by single molecules. The distance between Cy3 and Cy5 was estimated by the equation of $R = R_0(1/E - 1)^{1/6}$, with the R_0 value of 6 nm for the Cy3-Cy5 pair.

Bs Strains and Crosslinking

All strains are derivatives of *Bs* 1A700 (Bacillus Genetic Stock Centre). They were constructed and grown as described by Bürmann et al. (2013). A list of strains is presented in Table S1. In vivo crosslinking was performed as detailed by Bürmann et al. (2013).

Yeast Strain Construction and Protein Crosslinking

Yeast strains are derivatives of *Saccharomyces cerevisiae* W303. Genetic modifications of *SMC2* and *SMC4* loci were performed by double crossover recombination. Genotypes are listed in Table S2. Yeast protein extracts were incubated with Dynabeads Protein G charged with monoclonal SV5-Pk1 antibody. Beads were washed, resuspended, and treated with BMOE (0.5 mM) and incubated for 10 min on ice before quenching with 2-mercaptoethanol (2-ME, 14 mM).

Anisotropy Titration Measurements

Fluorescence anisotropy titrations were performed at 25°C using a BioTek Neo plate reader in a buffer containing 50 mM Tris-HCl at pH 7.5, 50 mM NaCl, and 3 mM $MgCl_2$ (plus 1 mM ATP) with 50 nM fluorescein-labeled dsDNA (40 bp).

Cysteine Crosslinking of *Bs* Smc and *Bs*SmcH-CC100

*Bs*SmcH-CC100 protein and double-stranded oligonucleotides (40 bp) were mixed at 4 μM and 20 μM, respectively, in 50 mM Tris, 50 mM NaCl, 2 mM $MgCl_2$, 0.25 mM TCEP (pH 7.5)/23°C (final). After incubation at room temperature for 5 min, BMOE was added (0.5 mM final). Reactions were incubated for 1 min at room temperature and quenched with 2-mercaptoethanol (14 mM). BMOE crosslinking of wild-type and mutant *Bs* Smc(A715C) (at 1 μM) was performed for 5 min at room temperature in the same buffer but with 3 mM $MgCl_2$, 10 μM DNA, with or without 1 mM ATP, and quenched with DTT in SDS loading buffer.

ACCESSION NUMBERS

The coordinates of the structures together with the structure factors have been deposited in the PDB: *Pf*SmcH-CC60 (4RSJ) and *Sc*Smc2H-CC110/*Sc*Smc4H-CC110 (4RSI).

SUPPLEMENTAL INFORMATION

Supplemental Information includes Supplemental Experimental Procedures, six figures, and three tables and can be found with this article online at http://dx.doi.org/10.1016/j.molcel.2014.11.023.

AUTHOR CONTRIBUTIONS

Y.-M.S. and H.-C.S. performed protein purification, structure determination, and biochemical experiments; F.B., *Sc* and *Bs* strain constructions and cellular and biochemical experiments; K.S.J., T.O., and M.S., SAXS conception and experiments; C.K., H.L., and N.K.L., FRET conception and experiments; S.J.K. and H.M.K., electron microscopy; Y.-G.K., X-ray data collection; C.P.T., DNA-binding measurements; M.-S.K. and M.-L.D.-D., protein purification; and Y.-M.S., F.B., H.-C.S., S.G., and B.-H.O., conception of experiments and preparation of the manuscript.

ACKNOWLEDGMENTS

The X-ray diffraction experiments used the Beamline 5C at the Pohang Accelerator Laboratory in Pohang, Korea, and the Beamline BL-17A at Photon Factory in Japan. We thank Dr. T. Hikima at SPring 8 for the help in SAXS data collection and Dr. M. Ikeguchi and Dr. Y. Kokabu for SAXS envelope models. We are grateful to J.-M. Peters for sharing results prior to publication and M. Dillingham for kindly providing expression plasmids and purification protocols for untagged *Bs* Smc protein. We thank Stefan Jentsch for sharing equipment and the Max Planck Institute of Biochemistry core facility for SEC-MALS analysis. This work was supported by the National Research Foundation of Korea (No. 2013-034955 to B.-H.O.), by the Intelligent Synthetic Biology Center of Global Frontier Project funded by the Ministry of Education, Science and Technology (No. 2011-0031955 to B.-H.O.), a European Research Council Starting Grant (DiseNtAngle #260853 to S.G.), and the Max Planck Society. The SAXS experiments were supported by the Platform for Drug Discovery, Informatics, and Structural Life Science from the Ministry of Education, Culture, Sports, Science and Technology, Japan.

Received: August 15, 2014
Revised: October 24, 2014
Accepted: November 19, 2014
Published: December 31, 2014

REFERENCES

Alipour, E., and Marko, J.F. (2012). Self-organization of domain structures by DNA-loop-extruding enzymes. Nucleic Acids Res. *40*, 11202–11212.

Anderson, D.E., Losada, A., Erickson, H.P., and Hirano, T. (2002). Condensin and cohesin display different arm conformations with characteristic hinge angles. J. Cell Biol. *156*, 419–424.

Arumugam, P., Gruber, S., Tanaka, K., Haering, C.H., Mechtler, K., and Nasmyth, K. (2003). ATP hydrolysis is required for cohesin's association with chromosomes. Current biology: CB *13*, 1941–1953.

Bürmann, F., Shin, H.C., Basquin, J., Soh, Y.M., Giménez-Oya, V., Kim, Y.G., Oh, B.H., and Gruber, S. (2013). An asymmetric SMC-kleisin bridge in prokaryotic condensin. Nat. Struct. Mol. Biol. *20*, 371–379.

Chiu, A., Revenkova, E., and Jessberger, R. (2004). DNA interaction and dimerization of eukaryotic SMC hinge domains. J. Biol. Chem. *279*, 26233–26242.

Cuylen, S., Metz, J., and Haering, C.H. (2011). Condensin structures chromosomal DNA through topological links. Nat. Struct. Mol. Biol. *18*, 894–901.

Fuentes-Perez, M.E., Gwynn, E.J., Dillingham, M.S., and Moreno-Herrero, F. (2012). Using DNA as a fiducial marker to study SMC complex interactions with the atomic force microscope. Biophys. J. *102*, 839–848.

Griese, J.J., and Hopfner, K.P. (2011). Structure and DNA-binding activity of the Pyrococcus furiosus SMC protein hinge domain. Proteins *79*, 558–568.

Griese, J.J., Witte, G., and Hopfner, K.P. (2010). Structure and DNA binding activity of the mouse condensin hinge domain highlight common and diverse features of SMC proteins. Nucleic Acids Res. *38*, 3454–3465.

Gruber, S., Arumugam, P., Katou, Y., Kuglitsch, D., Helmhart, W., Shirahige, K., and Nasmyth, K. (2006). Evidence that loading of cohesin onto chromosomes involves opening of its SMC hinge. Cell *127*, 523–537.

Gruber, S., Veening, J.W., Bach, J., Blettinger, M., Bramkamp, M., and Errington, J. (2014). Interlinked sister chromosomes arise in the absence of condensin during fast replication in B. subtilis. Current biology: CB *24*, 293–298.

Haering, C.H., Löwe, J., Hochwagen, A., and Nasmyth, K. (2002). Molecular architecture of SMC proteins and the yeast cohesin complex. Mol. Cell *9*, 773–788.

Haering, C.H., Schoffnegger, D., Nishino, T., Helmhart, W., Nasmyth, K., and Löwe, J. (2004). Structure and stability of cohesin's Smc1-kleisin interaction. Mol. Cell *15*, 951–964.

Hirano, T. (2012). Condensins: universal organizers of chromosomes with diverse functions. Genes Dev. *26*, 1659–1678.

Hirano, M., and Hirano, T. (2006). Opening closed arms: long-distance activation of SMC ATPase by hinge-DNA interactions. Mol. Cell *21*, 175–186.

Huis in 't Veld, P.J., Herzog, F., Ladurner, R., Davidson, I.F., Piric, S., Kreidl, E., Bhaskara, V., Aebersold, R., and Peters, J.M. (2014). Characterization of a DNA exit gate in the human cohesin ring. Science *346*, 968–972.

Hura, G.L., Menon, A.L., Hammel, M., Rambo, R.P., Poole, F.L., 2nd, Tsutakawa, S.E., Jenney, F.E., Jr., Classen, S., Frankel, K.A., Hopkins, R.C., et al. (2009). Robust, high-throughput solution structural analyses by small angle X-ray scattering (SAXS). Nat. Methods *6*, 606–612.

Kimura, K., and Hirano, T. (1997). ATP-dependent positive supercoiling of DNA by 13S condensin: a biochemical implication for chromosome condensation. Cell *90*, 625–634.

Ku, B., Lim, J.H., Shin, H.C., Shin, S.Y., and Oh, B.H. (2010). Crystal structure of the MukB hinge domain with coiled-coil stretches and its functional implications. Proteins *78*, 1483–1490.

Kurze, A., Michie, K.A., Dixon, S.E., Mishra, A., Itoh, T., Khalid, S., Strmecki, L., Shirahige, K., Haering, C.H., Löwe, J., and Nasmyth, K. (2011). A positively charged channel within the Smc1/Smc3 hinge required for sister chromatid cohesion. EMBO J. *30*, 364–378.

Li, Y., Schoeffler, A.J., Berger, J.M., and Oakley, M.G. (2010). The crystal structure of the hinge domain of the Escherichia coli structural maintenance of chromosomes protein MukB. J. Mol. Biol. *395*, 11–19.

Mascarenhas, J., Soppa, J., Strunnikov, A.V., and Graumann, P.L. (2002). Cell cycle-dependent localization of two novel prokaryotic chromosome segregation and condensation proteins in Bacillus subtilis that interact with SMC protein. EMBO J. *21*, 3108–3118.

Matoba, K., Yamazoe, M., Mayanagi, K., Morikawa, K., and Hiraga, S. (2005). Comparison of MukB homodimer versus MukBEF complex molecular architectures by electron microscopy reveals a higher-order multimerization. Biochem. Biophys. Res. Commun. *333*, 694–702.

Melby, T.E., Ciampaglio, C.N., Briscoe, G., and Erickson, H.P. (1998). The symmetrical structure of structural maintenance of chromosomes (SMC) and MukB proteins: long, antiparallel coiled coils, folded at a flexible hinge. J. Cell Biol. *142*, 1595–1604.

Moreno-Herrero, F., de Jager, M., Dekker, N.H., Kanaar, R., Wyman, C., and Dekker, C. (2005). Mesoscale conformational changes in the DNA-repair complex Rad50/Mre11/Nbs1 upon binding DNA. Nature *437*, 440–443.

Nasmyth, K. (2001). Disseminating the genome: joining, resolving, and separating sister chromatids during mitosis and meiosis. Annu. Rev. Genet. *35*, 673–745.

Nasmyth, K. (2011). Cohesin: a catenase with separate entry and exit gates? Nat. Cell Biol. *13*, 1170–1177.

Nolivos, S., and Sherratt, D. (2014). The bacterial chromosome: architecture and action of bacterial SMC and SMC-like complexes. FEMS Microbiol. Rev. *38*, 380–392.

Oldham, M.L., Davidson, A.L., and Chen, J. (2008). Structural insights into ABC transporter mechanism. Curr. Opin. Struct. Biol. *18*, 726–733.

Onn, I., Aono, N., Hirano, M., and Hirano, T. (2007). Reconstitution and subunit geometry of human condensin complexes. EMBO J. *26*, 1024–1034.

Rambo, R.P., and Tainer, J.A. (2010). Bridging the solution divide: comprehensive structural analyses of dynamic RNA, DNA, and protein assemblies by small-angle X-ray scattering. Curr. Opin. Struct. Biol. *20*, 128–137.

Rambo, R.P., and Tainer, J.A. (2013). Super-resolution in solution X-ray scattering and its applications to structural systems biology. Annual review of biophysics *42*, 415–441.

Revenkova, E., Focarelli, M.L., Susani, L., Paulis, M., Bassi, M.T., Mannini, L., Frattini, A., Delia, D., Krantz, I., Vezzoni, P., et al. (2009). Cornelia de Lange syndrome mutations in SMC1A or SMC3 affect binding to DNA. Hum. Mol. Genet. *18*, 418–427.

Schleiffer, A., Kaitna, S., Maurer-Stroh, S., Glotzer, M., Nasmyth, K., and Eisenhaber, F. (2003). Kleisins: a superfamily of bacterial and eukaryotic SMC protein partners. Mol. Cell *11*, 571–575.

Soppa, J., Kobayashi, K., Noirot-Gros, M.F., Oesterhelt, D., Ehrlich, S.D., Dervyn, E., Ogasawara, N., and Moriya, S. (2002). Discovery of two novel families of proteins that are proposed to interact with prokaryotic SMC proteins, and characterization of the Bacillus subtilis family members ScpA and ScpB. Mol. Microbiol. *45*, 59–71.

Thadani, R., Uhlmann, F., and Heeger, S. (2012). Condensin, chromatin crossbarring and chromosome condensation. Current biology: CB *22*, R1012–R1021.

Vos, S.M., Stewart, N.K., Oakley, M.G., and Berger, J.M. (2013). Structural basis for the MukB-topoisomerase IV interaction and its functional implications in vivo. EMBO J. *32*, 2950–2962.

Weitzer, S., Lehane, C., and Uhlmann, F. (2003). A model for ATP hydrolysis-dependent binding of cohesin to DNA. Curr. Biol. *13*, 1930–1940.

Williams, R.S., Williams, J.S., and Tainer, J.A. (2007). Mre11-Rad50-Nbs1 is a keystone complex connecting DNA repair machinery, double-strand break signaling, and the chromatin template. Biochemistry and cell biology *85*, 509–520.

Woo, J.S., Lim, J.H., Shin, H.C., Suh, M.K., Ku, B., Lee, K.H., Joo, K., Robinson, H., Lee, J., Park, S.Y., et al. (2009). Structural studies of a bacterial condensin complex reveal ATP-dependent disruption of intersubunit interactions. Cell *136*, 85–96.

Yamazoe, M., Onogi, T., Sunako, Y., Niki, H., Yamanaka, K., Ichimura, T., and Hiraga, S. (1999). Complex formation of MukB, MukE and MukF proteins involved in chromosome partitioning in Escherichia coli. EMBO J. *18*, 5873–5884.

Molecular Cell, Volume *57*

Supplemental Information

Molecular Basis for SMC Rod Formation and Its Dissolution upon DNA Binding

Young-Min Soh, Frank Bürmann, Ho-Chul Shin, Takashi Oda, Kyeong Sik Jin, Christopher P. Toseland, Cheolhee Kim, Hansol Lee, Soo Jin Kim, Min-Seok Kong, Marie-Laure Durand-Diebold, Yeon-Gil Kim, Ho Min Kim, Nam Ki Lee, Mamoru Sato, Byung-Ha Oh, and Stephan Gruber

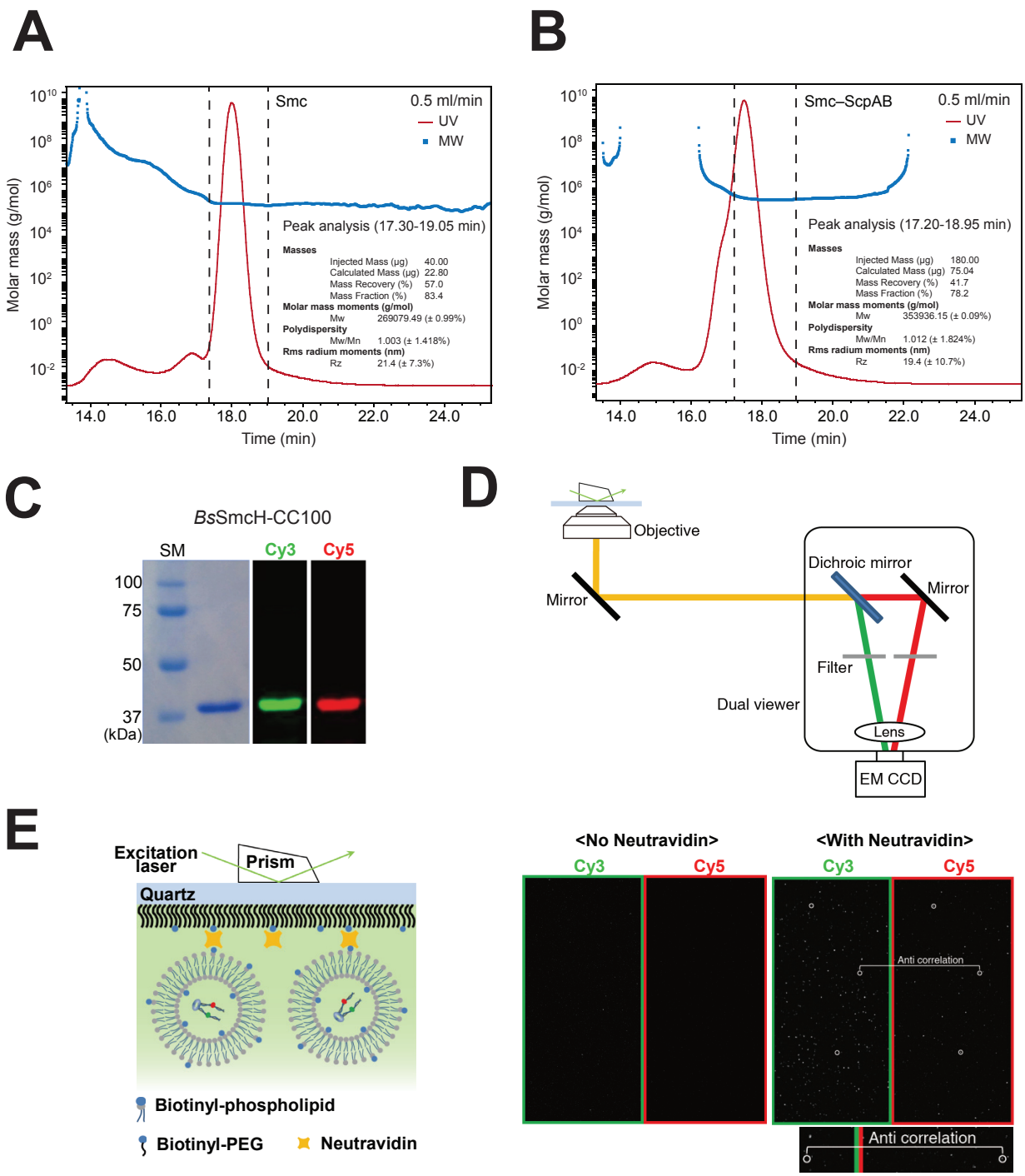

Figure S1

(Related to Figure 1)

Figure S1. SEC-MALS and FRET analysis of *Bs* Smc–ScpAB. Related to Figure 1.
(A) Purified fractions of *Bs* Smc were analyzed by size exclusion chromatography (Superdex 200 Increase 5/150) coupled to a multi angle light scattering detector (Wyatt Dawn TREOS-II). Molar mass (in g/mol) is plotted against the elution time from the size exclusion column (in min). The *Bs* Smc protein eluted from the size exclusion column as single peak at 18 min with an estimated molar mass of 269 kg/mol, which is consistent with it being a dimer (calculated molar mass: 271 kg/mol). Mw, weight-average molar mass; Mn, number-average molar mass.
(B) Same as in (A) with *Bs* Smc–ScpAB. The molar mass was calculated for the elution of the main peak between 17.2 and 18.95 min giving an estimate of 354 kg/mol, which is close to the calculated molar mass of a Smc_2–$ScpA_1$–$ScpB_2$ complex (345 kg/mol). In addition to this main peak a minor species eluted slightly earlier from the column.
(C) Cy3 and Cy5 labeling of *Bs*SmcH-CC100. The fluorescent band on a denaturing acrylamide gel confirms dual dye labeling. SM, size markers.
(D) Schematic drawing of the TIRF-FRET setup.
(E) Confirming vesicle immobilization. The immobilization strategy is shown in the left panel. Fluorescent signals (detecting Cy3 or Cy5 emission) in the presence of neutravidin confirmed immobilization of the vesicles containing dye-labeled *Bs*SmcH-CC100 (right panel). A vesicle containing a dye-labeled *Bs*SmcH-CC100 molecule appears as a single dot. The Cy3-Cy5 dimer exhibits both Cy3 and Cy5 signals as indicated by the circles. Because of FRET, the fluorescent signals of Cy3 and Cy5 are anti-correlated.
(F) FRET signals from single molecules were traced as a time course, and a representative one is shown. A high FRET state was maintained until the donor dye Cy3 was photobleached.
(G) FRET histogram of encapsulated *Bs*SmcH-CC100. A total of 123 time traces were analyzed that exhibited both donor and acceptor signals with single-step photobleaching.

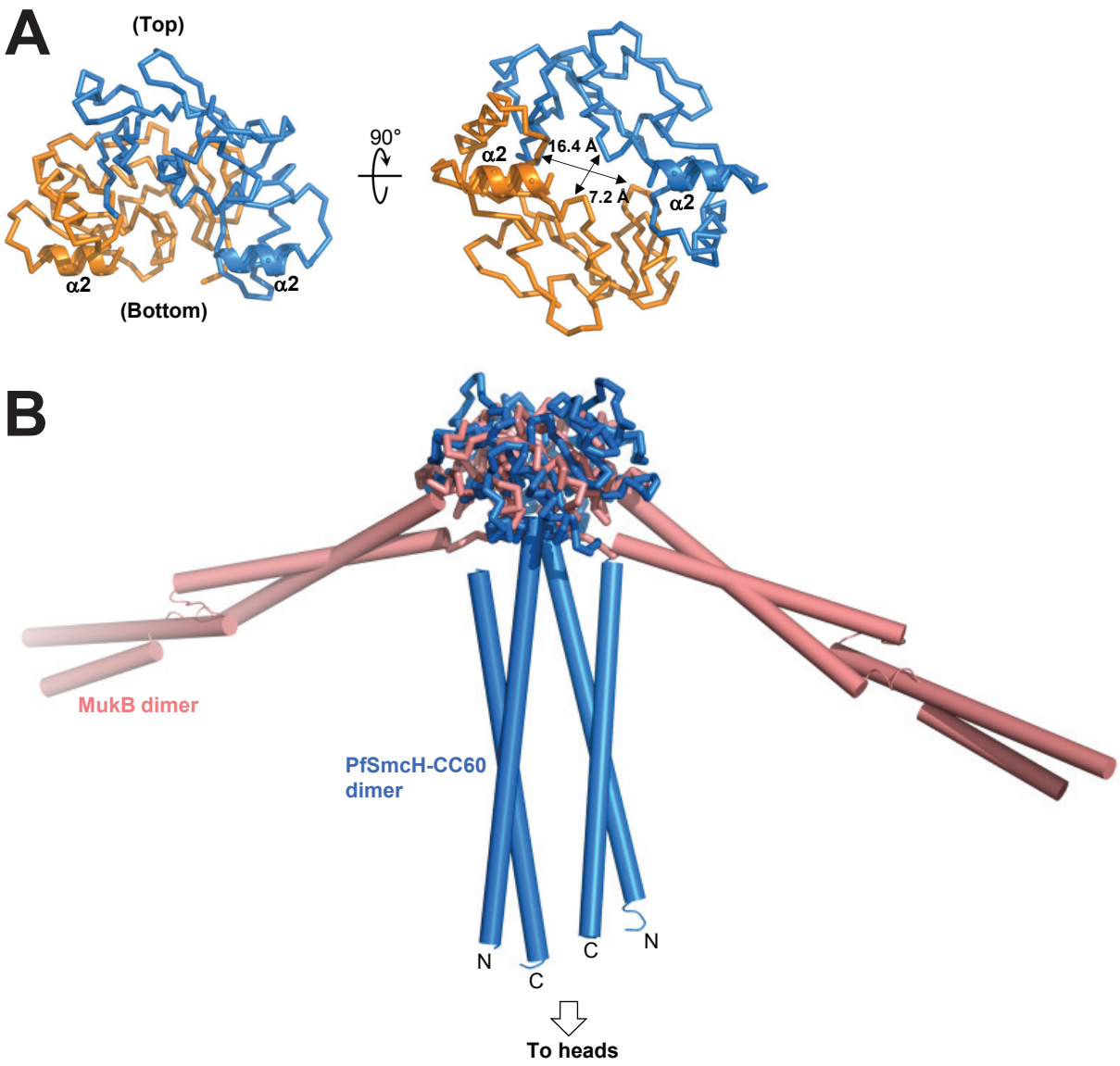

Figure S2

(Related to Figure 2)

Figure S2. Structural features of *Pf*SmcH-CC60. Related to Figure 2.

(A) The toroidal structure of the hinge domain homodimer. The coiled coils are omitted for clarity. A side and a top view are displayed on the left and right panel, respectively.

(B) Structural superposition of *Pf*SmcH-CC60 with a MukB hinge structure with long coiled coils (PDB entry: 3IBP).

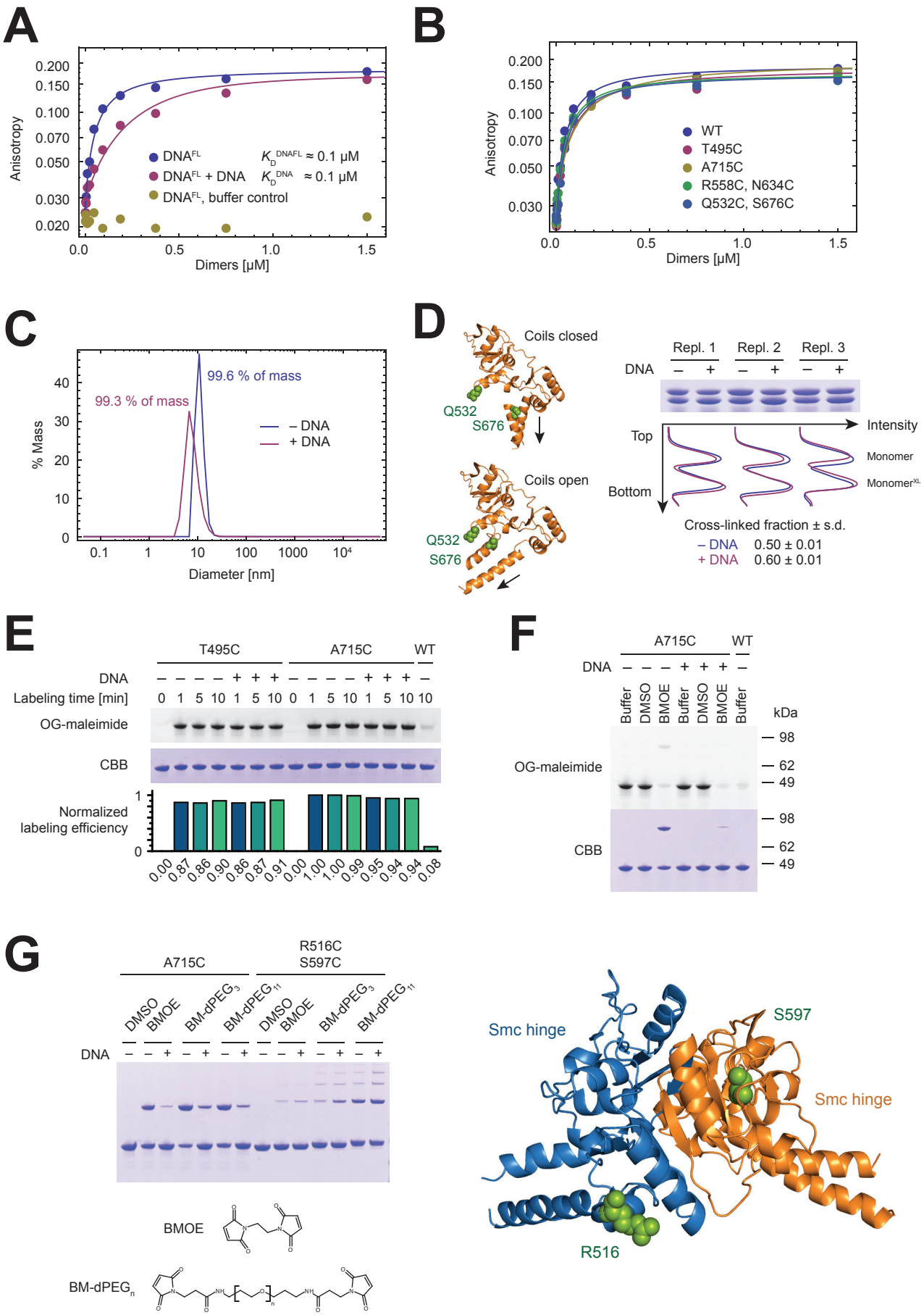

Figure S3

(Related to Figure 4)

Figure S3. Structural transition of the hinge-proximal coiled coil. Related to Figure 4.
(A) *Bs*SmcH-CC100 binds unlabeled DNA with similar affinity as fluorescein labeled DNA. Fluorescence anisotropy of 50 nM labeled double-stranded DNA (DNA^{FL}) was measured in the presence of 500 nM unlabeled DNA used for cross-linking experiments. Conditions were identical to those used for cross-linking experiments. Data were fitted with a competition model using K_D^{DNAFL} = 0.1 µM as a fixed parameter.
(B) DNA binding of *Bs*SmcH-C100 variants used in Fig. 4C. Buffer conditions were identical to those used for cross-linking experiments.
(C) *Bs*SmcH-CC100 forms defined complexes with DNA. Dynamic light scattering analysis of 6.5 µM protein in the presence or absence of 20 µM DNA under the same buffer conditions used for cross-linking experiments. Please note that scattering of free DNA is negligible.
(D) Structural transition at the coils/hinge interface. A model of *B. subtilis* Smc hinge conformations based on the *T. maritima* and *P. furiosus* structures predicts decreasing distance of Q532 and S676 residues upon coils opening (left panel). BMOE cross-linking analysis of *Bs*SmcH-CC100(Q532C, S676C) in the presence or absence of DNA (right panel). Bands were quantified by fitting densitograms (bottom right panel) with the sum of two skewed gaussians similar to the method of (Mitov et al., 2009).
(E) Cysteines in the *Bs*SmcH-CC100 coiled coil are reactive toward Oregon-Green maleimide in the presence of DNA. Labeling reactions were quenched at different time points and analysed by in-gel fluorescence and coomassie staining (CBB).
(F) A715C in the *Bs*SmcH-CC100 coiled coil is reactive toward BMOE in the presence of DNA. Cross-linking reactions were done as in Fig. 4C, except that an additional 1 min labeling step with Oregon-Green maleimide was included before quenching with 2-mercaptoethanol. CBB, coomassie brilliant blue.
(G) Cross-linking of *Bs*SmcH-CC100 cysteines with long cross-linkers. Predicted positions of R516 and S597 are shown in the right panel.

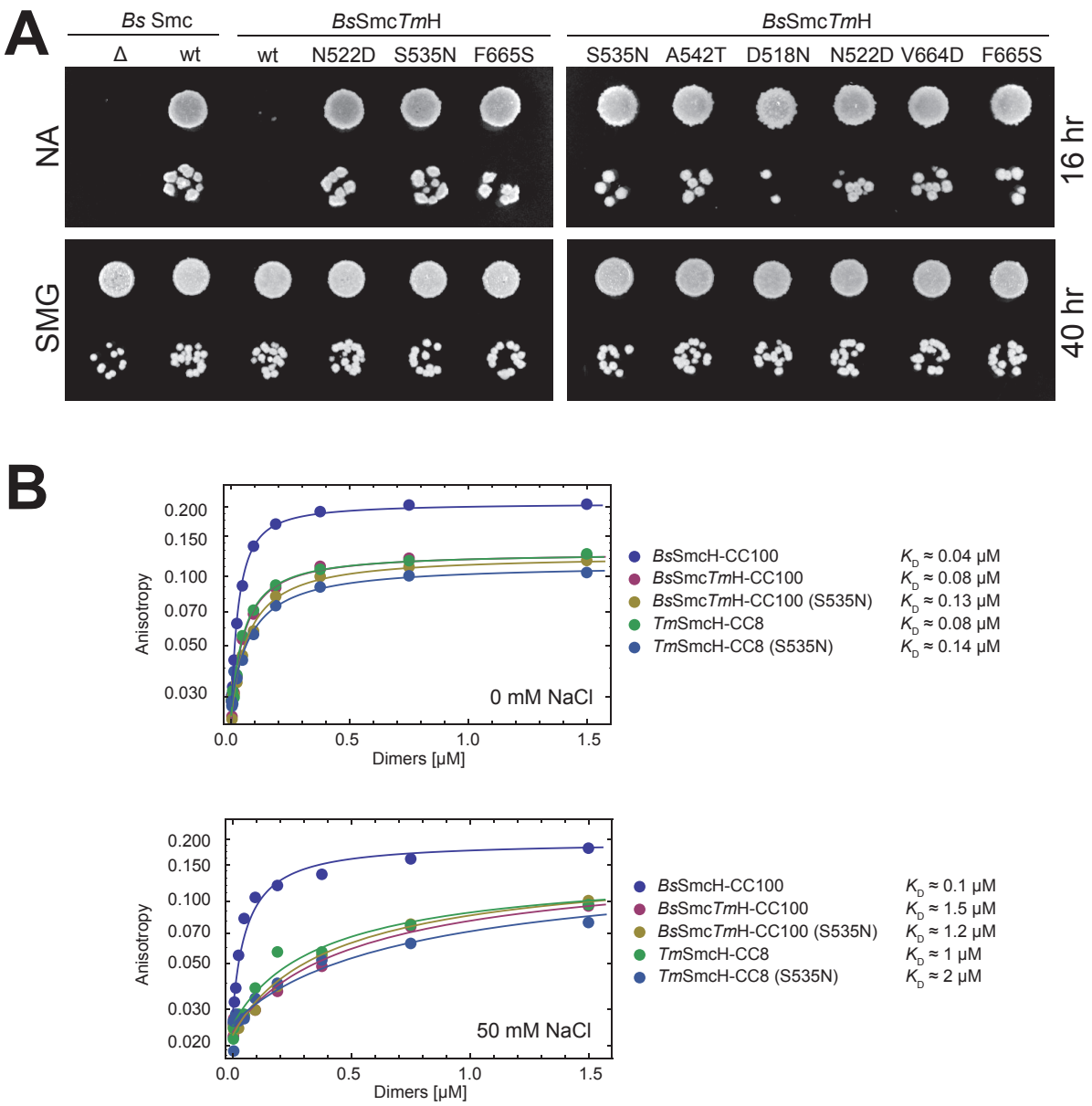

Figure S4

(Related to Figure 5)

Figure S4. Colony formation of *Bs* strains harboring chimeric Smc proteins. Related to Figure 5.

(A) Overnight cultures of strains (BSG1001, BSG1007, BSG1363, BSG1365-1368, BSG1966 and BSG1970) were serially diluted and spotted on nutrient agar (NA) or defined medium agar (SMG) and grown for 16 and 40 hr, respectively, at 37°C. Top left image is identical to figure panel 5A.

(B) DNA binding of *Bs*SmcH*Tm*H-CC100 chimeric constructs and *Tm*SmcH-CC8 hinges in buffer containing 0 mM NaCl or 50 mM NaCl. Former proteins contained C437S and A715C mutations.

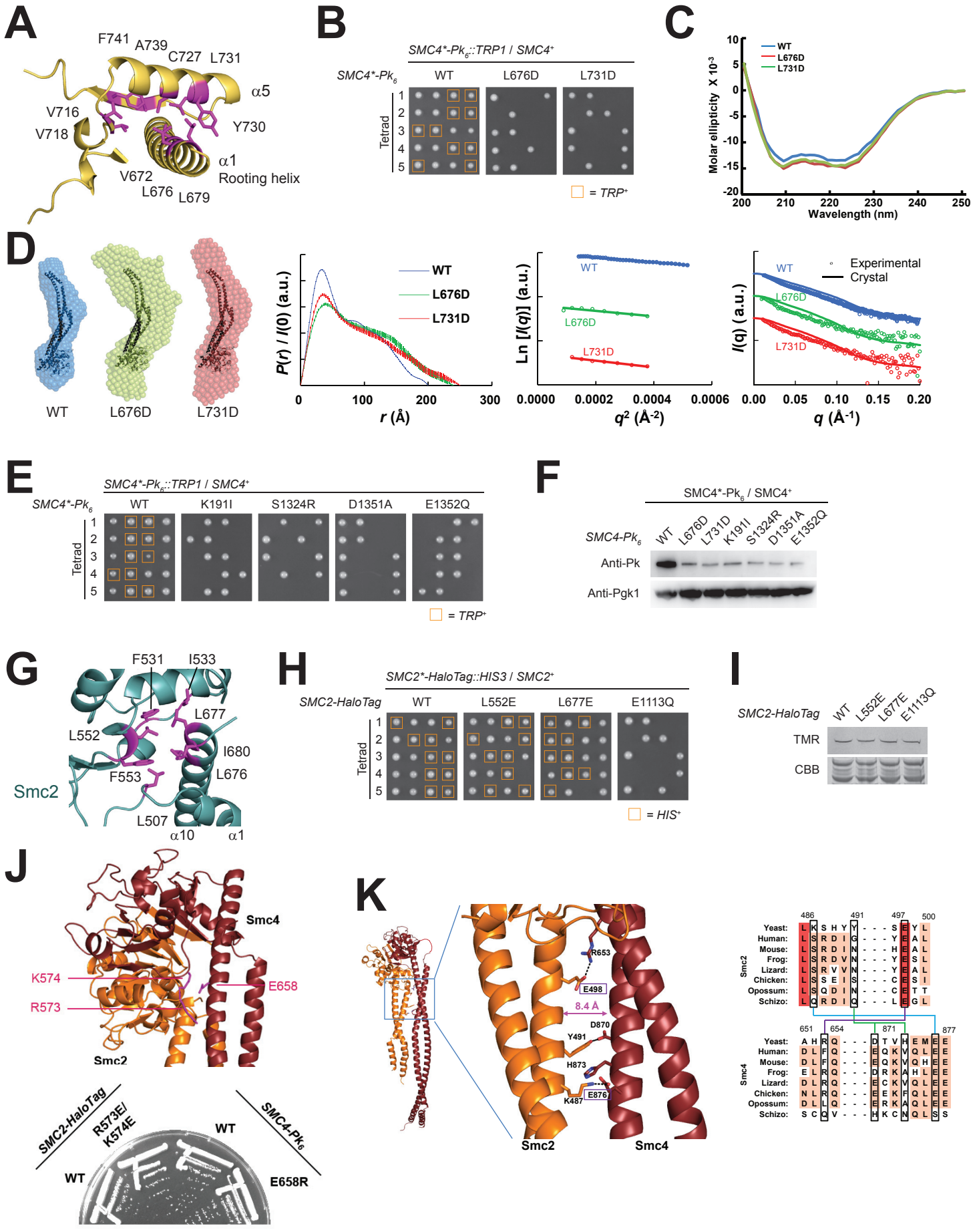

Figure S5

(Related to Figure 6)

Figure S5. Coils/coils and coils/hinge interactions at the yeast Smc2–4 condensin hinge. Related to Figure 6.

(A) Conserved residues at the Smc4 coils/hinge transition. Hydrophobic residues at the interface are display in stick representation in purple color. Same as Fig. 6C.

(B) Mutations in conserved residues on the Smc4 rooting helix are lethal in yeast. Tetrad dissection analysis of diploid yeast strains heterozygous for SMC4 genes. Spores of five tetrads were outgrown on YPAD at 30 °C and segregation of the modified alleles was monitored by testing for tryptophan prototrophy (orange box). Yeast strains: YSG079, YSG163 and YSG164.

(C) CD spectra of wild-type and mutant *Sc*Smc2H-CC110–*Sc*Smc4H-CC110 complexes.

(D) Dummy atom models for wild-type and mutant *Sc*Smc2H-CC110–*Sc*Smc4H-CC110 complexes based on SAXS measurements. The overall shapes of the mutant complexes are similar to the wild type but slightly more extended. *P(r)* graphs, Guinier plots and SAXS curves are shown. The discrepancies (χ^2) between the experimental *I*(*q*) curves and the theoretical *I*(*q*) curve calculated from the crystal structure of *Sc*Smc2H-CC110–*Sc*Smc4H-CC110 are WT = 32.16, L676D = 9.71, L731D = 10.36. Please note that the crystal structure of *Sc*Smc2H-CC110–*Sc*Smc4H-CC110 (PDB entry: 4RSI) contains only about half of the Smc2 coiled coil present in the *Sc*Smc2H-CC110–*Sc*Smc4H-CC110 construct.

(E) Smc4 ATPase mutations are lethal in yeast. As in (B), but SMC4-Pk$_6$ ATPase mutants were tested. K191I and D1351A block ATP binding, S1324R blocks head engagement, E1352Q blocks ATP hydrolysis. Yeast strains: YSG079, YSG172, YSG173, YSG174 and YSG175 (left).

(F) Smc4 mutant proteins are poorly expressed in yeast. Immunoblot analysis of strains shown in (B) and (E). The membrane was probed for Smc4-Pk$_6$ and Pgk1 as a loading control.

(G) Conserved residues at the Smc2 coils/hinge transition. Hydrophobic residues at the interface are display in stick representation in purple color. Same image as Figure 6C.

(H) Mutations at the Smc2 coils/hinge interface are not lethal. Tetrad dissection analysis of diploid yeast strains heterozygous for SMC2-HaloTag genes. Spores of tetrads were outgrown on YPAD at 30 °C and segregation of the modified alleles was monitored by testing for histidine prototrophy (orange box). Only the ATP hydrolysis defective Smc2(E1173Q) mutant is lethal. Yeast strains: YSG186-189.

(I) Smc2 mutant proteins are expressed at normal levels in yeast.
(J) Non-essential interactions between the Smc4 coiled coil and the Smc2 hinge domain. Contact between Arg573 and Lys574 in the Smc2 hinge and Glu658 on the Smc4 coiled coil (top). Yeast strains (YSG070, YSG143, YSG144 and YSG145) containing the charge reversal mutations, Smc2(R573E, K574E) and Smc4(E658R), were viable when grown on YPAD medium at 30 °C for 24 h (bottom).
(K) Interactions between Smc2 and Smc4 coiled coils. The interacting residues are shown in stick representation. The closest separation between the two helices is shown, which is much wider (>8 Å) than the ~5 Å separations in the *Pf* Smc (Fig 2C). Conserved residues (>80%) are indicated by rectangular boxes. The interacting pairs are linked by lines on the multiple sequence alignment. None of these exhibit obvious pairwise conservation.

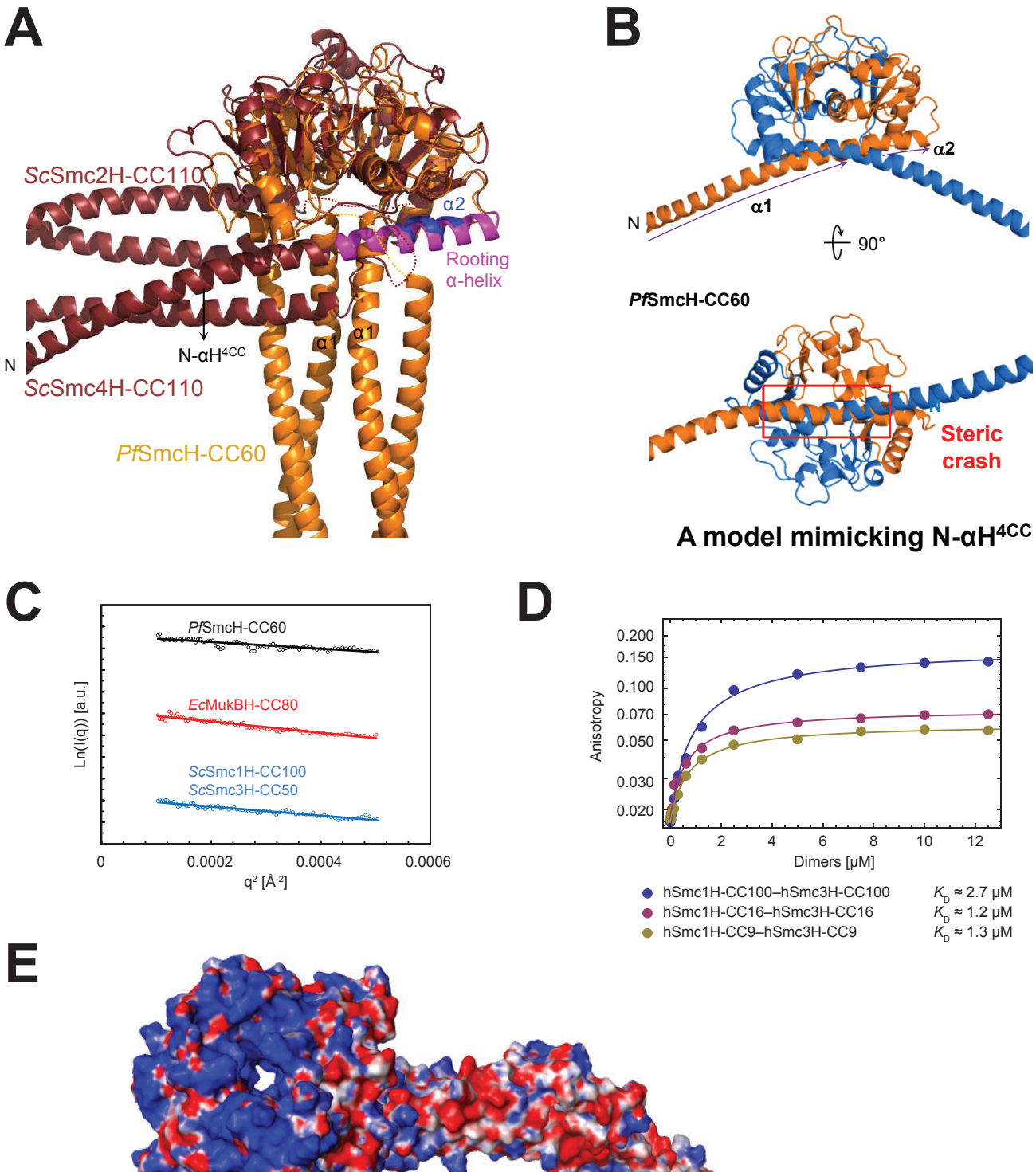

Figure S6

(Related to Figure 7)

Figure S6. Structural comparison of the symmetric and asymmetric coils/hinge organization in Smc–ScpAB and condensin. Related to Figure 7.

(A) Superimposition of the structures *Pf*SmcH-CC60 and *Sc*Smc2-CC110–*Sc*Smc4H-CC110 shows structural overlap of the rooting helix α2 in *Pf*SmcH-CC60 (displayed in blue color) with the rooting helix α1 in Smc4 (displayed in pink color).

(B) Modeling. The molecular symmetry prevents α1 and α2 of the *Pf* Smc hinge from forming a single continuous α-helix. The C-terminal coiled-coil helix is omitted for clarity.

(C) Guinier plots of the SAXS experiments shown in Figure 7.

(D) DNA binding of the human cohesin hinge with different lengths of coiled coil. Fluorescence anisotropy of fluorescein labeled DNA (40 bp) was measured.

(E) Electrostatic potential map of the *Sc*Smc2H-CC110–*Sc*Smc4H-CC110 dimer displayed from -6 k_BT/e (red) to +6 k_BT/e (blue).

SUPPLEMENTAL TABLES

Table S1. Genotypes of *Bacillus subtilis* strains

Name	Genotype
BSG1001	*Bacillus subtilis 1A700, trpC2*
BSG1007	*trpC2, Δsmc ftsY::ermB*
BSG1363	*trpC2, smcTmHinge ftsY::specR*
BSG1365	*trpC2, smcTmHinge(S535N) ftsY::specR*
BSG1366	*trpC2, smcTmHinge(A542T) ftsY::specR*
BSG1367	*trpC2, smcTmHinge(D518N) ftsY::specR*
BSG1368	*trpC2, smcTmHinge(N522D) ftsY::specR*
BSG1711	*trpC2, smc-tev-halotag ftsY::ermB*
BSG1760	*trpC2, smc(D491C)-tev-halotag ftsY::ermB*
BSG1761	*trpC2, smc(M492C)-tev-halotag ftsY::ermB*
BSG1762	*trpC2, smc(T495C)-tev-halotag ftsY::ermB*
BSG1763	*trpC2, smc(Q708C)-tev-halotag ftsY::ermB*
BSG1764	*trpC2, smc(K712C)-tev-halotag ftsY::ermB*
BSG1765	*trpC2, smc(A715C)-tev-halotag ftsY::ermB*
BSG1821	*trpC2, smc(D716C)-tev-halotag ftsY::ermB*
BSG1822	*trpC2, smc(E719C)-tev-halotag ftsY::ermB*
BSG1823	*trpC2, smc(E722C)-tev-halotag ftsY::ermB*
BSG1921	*trpC2, smc(C119S, C437S, A715C, C826S, C1114S)-tev-his-halotag (C61V, C262A) ftsY::ermB*
BSG1932	*trpC2, smc(C119S, C437S, TmHinge, A715C, C826S, C1114S)-tev-his-halotag (C61V, C262A) ftsY::ermB*
BSG1934	*trpC2, smc(C119S, C437S, TmHinge(S535N), A715C, C826S, C1114S)-tev-his-halotag(C61V, C262A) ftsY::ermB*
BSG1966	*trpC2, smcTmHinge(V664D) ftsY::ermB*
BSG1970	*trpC2, smcTmHinge(F665S) ftsY::ermB*

Table S2. Genotypes of yeast strains

Name	Genotype
YSG006	*Saccharomyces cerevisiae* W303, MATa
YSG008	*Saccharomyces cerevisiae* W303, MATa/α
YSG070	W303, MATa, SMC4-Pk6::TRP1
YSG079	W303, MATa/α, SMC4/SMC4-Pk6::TRP1
YSG081	W303, MATa, SMC2-HaloTag::HIS3, SMC4-Pk6::TRP1
YSG099	W303, MATa, SMC2(N506C)-HaloTag::HIS3, SMC4(Q654C)-Pk6::TRP1
YSG100	W303, MATa, SMC2(C494S, E498C)-HaloTag::HIS3, SMC4(E862C)-Pk6::TRP1
YSG101	W303, MATa, SMC2(C494S, K495C)-HaloTag::HIS3, SMC4(R866C)-Pk6::TRP1
YSG102	W303, MATa, SMC2(K487C, C494S)-HaloTag::HIS3, SMC4(E876C)-Pk6::TRP1
YSG143	W303, MATa, SMC2(R573E, K574E)-HaloTag::HIS3
YSG144	W303, MATa, SMC4(E658R)-Pk6::TRP1
YSG145	W303, MATa, SMC2-HaloTag::HIS3
YSG158	W303, MATa, SMC2(K487C, C494S)-HaloTag::HIS3, SMC4(Q654C)-Pk6::TRP1
YSG163	W303, MATa/α, SMC4(L676D)-Pk6::TRP1/SMC4
YSG164	W303, MATa/α, SMC4(L731D)-Pk6::TRP1/SMC4
YSG172	W303, MATa/α, SMC4(K191I)-Pk6::TRP1/SMC4
YSG173	W303, MATa/α, SMC4(S1324R)-Pk6::TRP1/SMC4
YSG174	W303, MATa/α, SMC4(D1341A)-Pk6::TRP1/SMC4
YSG175	W303, MATa/α, SMC4(E1352Q)-Pk6::TRP1/SMC4
YSG186	W303, MATa/α, SMC2-HaloTag::HIS3/SMC2
YSG187	W303, MATa/α, SMC2(L552E)-HaloTag::HIS3/SMC2
YSG188	W303, MATa/α, SMC2(L677E)-HaloTag::HIS3/SMC2
YSG189	W303, MATa/α, SMC2(E1113Q)-HaloTag::HIS3/SMC2
YSG192	W303, MATa, SMC2(C494S, Q681C)-HaloTag::HIS3, SMC4(Q654C)-Pk6::TRP1
YSG193	W303, MATa, SMC2(C494S, Q685C)-HaloTag::HIS3, SMC4(E862C)-Pk6::TRP1
YSG194	W303, MATa, SMC2(C494S, K688C)-HaloTag::HIS3, SMC4(R866C)-Pk6::TRP1

Table S3. SAXS derived parameters. Related to Figures 7.

Proteins	R_g (Å)	D_{max} (Å)	$Mass_{SAXS}$ (kDa)	$Mass_{Sequence}$ (kDa)
*Pf*SmcH-CC60	40 ± 1	134	58.9	61.6
*Ec*MukH-CC80	68 ± 1	239	68.3	68.1
*Sc*Smc1H-CC100–*Sc*Smc3H-CC50	56 ± 1	185	71.8	77.0
*Sc*Smc2H-CC110–*Sc*Smc4H-CC110	59 ± 1	200	104	90.5
*Sc*Smc2H-CC110–*Sc*Smc4H-CC110(L676D)	68 ± 4	240	125	90.5
*Sc*Smc2H-CC110–*Sc*Smc4H-CC110(L671D)	68 ± 4	250	113	90.5

The radius of gyration (R_g) was derived from the equation $I(q)= I(0) \exp(-q^2R_g^2/3)$; the maximum diameter ($D_{max}$) from $P(r)$; molecular mass from the absolute $I(0)$ intensity or from the scattering curve ($q< 0.2$) based on Q_R ($Mass_{SAXS}$) (Rambo and Tainer, 2013). R_g, D_{max} and $Mass_{SAXS}$ of *Sc*Smc2H-CC110–*Sc*Smc4H-CC110 (WT) were calculated from the $I(q)$ curve extrapolated to infinite dilution. Those of mutants were calculated from the $I(q)$ curve at one protein concentration: 1 mg/mL (L676D) and 1.2 mg/mL (L731D). The experimental *I(q)* curve of *Pf*SmcH-CC60, *Ec*MukBH-CC80 and *Sc*Smc1H-CC100–*Sc*Smc3H-CC100 were measured at 4.0, 6.0 and 1.9 mg/mL, respectively.

SUPPLEMENTAL EXPERIMENTAL PROCEDURES

Purification of *Pf*SmcH-CC60

The DNA fragment encoding *P. furiosus* Smc residues 445-720 was ligated into pET-22b-CPD 10H, a modified pET-22b plasmid (Novagen) to express target protein with a C-terminal fusion of a His_{10}-tagged cysteinyl protease domain (CPD) derived from *Vibrio cholerae* (Shen et al., 2009). Each of the two proteins was expressed in *E. coli* BL21(DE3) RIPL strain (Novagen). Cell lysate prepared in Buffer A was heat treated in a 80 ^{o}C water bath for 30 min. The resulting supernatant was loaded onto a column containing HisPur^{TM} Co resin, and the resin was equilibrated with Buffer A containing additional 1 mM inositol hexakisphosphate for 1 h at 4 ^{o}C to cleave off the CPD-$(His)_{10}$ tag. *Pf*SmcH-CC60 was further purified using a Hitrap Q column and a HiLoad 26/60 Superdex 200 column.

Purification of *Sc*Smc2H-CC110–*Sc*Smc4H-CC110

The DNA fragments encoding yeast Smc2 residues 396-792 and yeast Smc4 residues 555-951 were inserted into a modified pRSFDuet-1 vector by standard PCR-based cloning methods. *Sc*Smc2H-CC110 with an N-terminal $(His)_{10}$-tag and *Sc*Smc4H-CC110 without a tag were co-expressed in the *E. coli* BL21(DE3) RIPL strain (Novagen). Cell lysate was applied onto a gravity flow column containing HisPur^{TM} Cobalt Resin (Thermo Scientific). The column was washed with Buffer A containing 20 mM Tris-HCl (pH 7.5), 0.1 *M* NaCl and 3 mM β-mercaptoethanol (β-ME), and the complex was eluted with Buffer A containing additional 150 m*M* imidazole. After TEV protease treatment overnight the complex was further purified using a Hitrap Q anion exchange column (GE Healthcare) and HiLoad 26/60 Superdex 200 gel filtration column (GE Healthcare). Initially, selenomethionine (SelMet) was incorporated into both proteins, but the resulting complex yielded only poorly diffracting crystals. Subsequently, SelMet was incorporated only into *Sc*Smc4H-CC110. For separate production of the two proteins, the DNA fragment encoding *Sc*Smc4H-CC110 was cloned into pET-30a (Novagen) and that encoding *Sc*Smc2H-CC110 into pProExHTa (Invitrogen). SelMet-substituted *Sc*Smc4H-CC110 was expressed in *E.coli* B834(DE3) RIL (Novagen), and native *Sc*Smc2H-CC110 was expressed in *E. coli* BL21(DE3) RIPL strain. The cells obtained from the two different

cultures were co-sonicated, and the half labeled SelMet-complex was purified in the same way as the native protein complex.

Purification of *Bs*SmcH-CC100

The DNA fragment encoding *B. subtilis* Smc residues 400-776 was ligated into the pET-22b-CPD 10H vector. The protein was expressed in the *E. coli* BL21 (DE3) RIPL strain at 18 ^{o}C. Bacterial cell lysate was prepared by sonication in Buffer A and loaded onto a column containing HisPur^{TM} Co resin (Thermo Scientific). After on-gel digestion reaction with 1 mM inositol hexakisphosphate to cleave off the CPD-$(His)_{10}$ tag, *Bs*SmcH-CC100 was further purified using a HitrapQ column and a HiLoad 26/60 Superdex 200 gel-filtration column. The final sample was concentrated up to 20 mg/ml using a Amicon Ultra centrifugal filter.

Purification of *B. subtilis* Smc–ScpAB

The DNA fragment encoding *B. subtilis* Smc was ligated into pET-22b, and those encoding ScpA and ScpB into a modified pRSF Duet vector. The three proteins were coexpressed in the *E. coli* BL21(DE3) strain at 18 ^{o}C. Bacterial cell lysate was prepared by sonication in Buffer A with 0.35 M NaCl and loaded onto a column containing HisPur^{TM} Co resin. The column was equilibrated with Buffer A with 0.35 M NaCl and 1 mM inositol hexakisphosphate for 1 h at 4 ^{o}C to cleave off the CPD-$(His)_{10}$ tag. The complex was further purified using a Hitrap Q anion exchange column and HiLoad 26/60 Superdex 200 gel filtration column. The final buffer contained 20 mM HEPES pH 7.5, 0.35 M NaCl, 10% Glycerol, 1 mM EDTA, and 1 mM DTT.

Purification of *B. subtilis* Smc and Smc(A715C)

Wild-type *Bs* Smc and cysless Smc(A715C) protein was expressed and purified as described in (Fuentes-Perez et al., 2012) with an additional Superose 6 10/300 GL (GE Healthcare) gel filtration added as a final step in the purification. Gel filtration was performed in storage buffer 50 mM Tris-HCl at pH 7.5, 150 mM NaCl, and 1 mM DTT.

Purification of *Bs*SmcH

*Bs*SmcH (residues 498-665) was cloned into pET-22b. Expression was performed in

Escherichia coli BL21 (DE3) Gold for 14 hr at 27 °C. The full-length Smc protocol was followed for the first Blue Sepharose FF column (GE Healthcare). Peak fractions were then run on Superdex 200 10/300 GL gel filtration (GE Healthcare) in storage buffer.

Purification of *Bs*SmcH-CC8-His6

The *Bs* Smc hinge with short coiled coils (residues 489-680) was fused to a C-terminal HISx6-CYS tag and cloned into pET-28 (to yield plasmid pSG1530). The protein was expressed in *E. coli* BL21 (DE3) Gold in auto-induction medium (overnight express TB broth, Novagen) at 25°C for 24 hr and purified in two steps via a HisTrap column (GE Healthcare) and by gel filtration (Superdex 200 10/300 GL) into storage buffer.

Purification of His6-*Bs*SmcH-CC100 for cross-linking analysis

His6-*Bs*SmcH-CC100 constructs containing the C437S mutation were produced from pET-28 derived vectors in *E. coli* BL21-Gold (DE3) for 24 h at 24 °C using auto-induction medium (OvernightExpress TB, Novagen). Extracts were prepared by sonication in 50 mM NaPi, pH 7.4 / 4 °C, 300 mM NaCl, 80 mM imidazole, 10 % glycerol, 1 mM DTT and bound to Ni^{2+} Sepharose FF (GE Healthcare). Columns were washed with 10 column volumes (CV) of binding buffer, followed by 5 CV of 50 mM NaPi, pH 7.4 / 4 °C, 1 M NaCl, 10 % glycerol, 1 mM DTT, followed by 5 CV of binding buffer. Proteins were eluted with 500 mM imidazole, pH 7.4 / 4 °C, 300 mM NaCl, 10 % glycerol, 1 mM DTT and further purified on Superdex 200 in 50 mM Tris-HCl, 200 mM NaCl, 1 mM TCEP, pH 7.4 / 4 °C (final). Aliquots were flash frozen in liquid N_2 and stored at -80 °C.

Purification of *Bs*SmcH-CC300

*Bs*SmcH-CC300 (residues 188-1011) with an N-terminal His-TEVs tag was purified under similar conditions as His6-*Bs*SmcH-CC100, except that an additional TEV protease cleavage step was included.

Purification of *Ec*MukBH-CC80

The DNA fragment encoding *E. coli* MukB residues 566-863 was ligated into a modified pProEx HTa vector containing a $(His)_{10}$ tag. The protein was expressed in the *E. coli* BL21 (DE3) strain at 18 °C. Bacterial cell lysate was prepared by sonication in Buffer

containing 20 mM Tris-HCl (pH 7.5), 0.45 M NaCl and 3 mM β-ME, and loaded onto a column containing HisPur^{TM} Co resin. The protein was eluted with Buffer A containing additional 150 mM imidazole. After TEV protease treatment overnight, the protein was further purified using a Hitrap Q anion exchange column and HiLoad 26/60 Superdex 200 gel filtration column. The *Ec*MukBH-CC80 variant containing a C730A mutation, which was used for FRET analysis, was expressed and purified in the same manner as the wild-type version of the protein.

Purification of *Sc*Smc1H-CC100 and *Sc*Smc3H-CC50

The DNA fragments encoding yeast Smc1 residues 399-794 and Smc3 residues 467-743 were ligated into a pET-30a (Novagen) and pProExHTa (Invitrogen) vector, respectively. The two proteins were co-expressed in the *E. coli* BL21 (DE3) RIPL codon plus strain at 18 ^{o}C. The protein complex was purified in the same manner as *Sc*Smc2H-CC110–*Sc*Smc4H-CC110.

Purification of human Smc1–3 hinge complexes

The DNA fragments encoding human Smc1 residues 499-675, 471-685 or 382-784 were ligated into the pET-30a vector. The DNA fragments encoding Smc3 residues 492-685, 484-696 or residues 400-774 were ligated into the pProExHTa vector. Three pairs of the proteins, Smc1(499-675) and Smc3(492-685) (=hSmc1H-CC9–Smc3H-CC9), Smc1(471-685) and Smc3(484-696) (=hSmc1H-CC16–hSmc3H-CC16) and Smc1(382-784) and Smc3(400-774) (=hSmc1H-CC100–hSmc3H-CC100), were co-expressed in the *E. coli* BL21 (DE3) RIPL strain at 18 °C. The protein complexes were purified in the same manner as *Sc*Smc2H-CC110–*Sc*Smc4HCC110.

Crystallization, X-ray data collection and structure determination

Initial crystals of *Pf*SmcH-CC60 (40 mg/ml) were obtained by the sitting-drop vapor-diffusion method at 22 °C in a precipitant solution containing 1 M sodium citrate and 0.2 M CHES (pH 9.5). Larger single crystals were grown by the hanging-drop vapor-diffusion method at 22 °C from a precipitant solution containing 1 M sodium citrate, 0.1 M CHES (pH 9.5) and 8% glycerol. The *Sc*Smc2H-CC110–*Sc*Smc4H-CC110 complex (20 mg/ml) was crystallized using the hanging-drop vapor diffusion technique at 20 °C in a

precipitant solution containing 16% PEG 300, 0.1 *M* Na/K phosphate pH 6.0, 8% glycerol and 10 m*M* dithiothreitol (DTT). The SelMet-substituted complex was crystallized under the same crystallization condition. X-ray diffraction data were collected at the beamline BL17A at the Photon Factory, Japan and the beamline 5C at the Pohang Accelerator Laboratory, Korea. A native data set was collected for *Pf*SmcH-CC60. A single-wavelength anomalous dispersion (SAD) data set was collected with a SelMet-substituted *Sc*Smc2H-CC110–*Sc*Smc4H-CC110 crystal at the Se absorption peak. Obtaining good data set for the *Sc*Smc2H-CC110–*Sc*Smc4H-CC110 crystal was exhausting at its thin crystal easily bent due to minor crystal contacts in one direction. All diffraction data were processed with HKL2000 (Otwinowski and Minor, 1997). The structure of *Pf*SmcH-CC60 was determined by molecular replacement using the structure of the coiled coil-less *Pf* Smc hinge (PDB entry: 3NWC) as a probe by using the program Phenix AutoMR (McCoy et al., 2007). The *Sc*Smc2H-CC110–*Sc*Smc4H-CC110 structure was solved by the single isormorphous replacement with anomalous scattering (SIR-AS) method. The model building and structure refinement were carried out using the programs *COOT* (Emsley and Cowtan, 2004) and *CNS* (Brunger et al., 1998). The final model of *Sc*Smc2H-CC110–*Sc*Smc4H-CC110 does not include residues 671-673 of Smc2 and 836-841 of Smc4, which are disordered in the crystals. Crystallographic data statistics are summarized in Table 1.

SAXS analysis

SAXS data were collected on the BL45XU beamline SPring8 (for *Sc*Smc2H-CC110–*Sc*Smc4H-CC110) and a BioSAXS-1000 system (for mutants thereof) and on the 4C SAXS II beamline at Pohang Light Source II (for *Pf*SmcH-CC60, *Ec*MukBH-CC80 and *Sc*Smc1H-CC100–*Sc*Smc3H-CC50). The PILATUS300k-w detector on the BL45XU beamline, at a sample-to-detector distance of 3496 mm, was used to measure scattering intensities at 20 °C. The SX165 detector on the 4C SAXS II beamline, at a sample-to-detector distance of 2000 or 4000 mm, was used to measure scattering intensities at 4 °C. Samples of varying protein concentrations were used to obtain triplicate measurements per each sample with an exposure time 30 to 60 sec at 0.675 Å or 1.000 Å wavelength. The data were processed and analyzed using the software applications embedded in the ATSAS package [http://www.embl-hamburg.de/biosaxs/software.html].

The one-dimensional scattering data $I(q)$ as a function of q ($q = 4\pi\sin\theta/\lambda$, where 2θ is the scattering angle and λ is the wavelength) was obtained through radial averaging. Scattering intensities from the buffer solution were measured and used for background subtraction. The $I(q)$ data of the samples were then extrapolated to zero concentration. The program GNOM was used to calculate the distance distribution function $P(r)$. The maximum dimension (D_{max}) of the particle, was determined from the $P(r)$ function, the distance r where $P(r) = 0$. Molecular envelope models were produced by program DAMMIF (Franke and Svergun, 2009). Six independently calculated, low-resolution dummy atom models were averaged by program DAMAVER (Volkov and Svergun, 2003). Superposition of the molecular envelopes and crystal structures was carried out by program SUPCOMB (Kozin and Svergun, 2001). SAXS data for the *Sc*Smc2H-CC110–*Sc*Smc4H-CC110 mutants were collected with BioSAXS-1000 (Rigaku) mounted on a MicroMax007HF X-ray generator (Rigaku). The PILATUS100k detector, at a sample-to-detector distance 484 mm, was used to measure scattering intensities at 20 °C. The protein concentration was 1 mg/mL and 1.2 mg/mL for the L676D and the L731D mutant, respectively. Quadruple measurements were obtained per each sample with 1 h exposure at 1.5418 Å wavelength.

ALEX-FRET and TIRF-FRET analyses

The BsSmcH-CC100 homodimer was labeled with Cy3- and Cy5-maleimide (GE Healthcare). For dual labeling, the two fluorescent dyes were added at a 1:2 (protein:dye) molar ratio. The mixture was incubated for 6 h at 4 ^{o}C. Unreacted dyes were removed by a PD minitrap G-25 size-exclusion column (GE healthcare). The dye labeling was confirmed by a fluorescent protein band on a SDS-PAGE gel. The reaction mixture containing three types of products, Cy3-BsSmcH-CC100-Cy3 (donor only), Cy5-BsSmcH-CC100-Cy5 (acceptor only) in addition to Cy3-BsSmcH-CC100-Cy5 (FRET pair), was used for single-molecule techniques. The ALEX-FRET method and data analysis were described in previous works (Kim et al., 2012; Lee et al., 2005). The laser intensities for donor and acceptor excitation were 80 μW and 35 μW, respectively. In order to detect single-diffusing molecule in solution, the protein sample was diluted approximately to 50 pM in a buffer solution containing 20 mM Tris-HCl (pH 7.5), 100 mM NaCl, 1 mM NaN_3, 1 mM DTT, 5% glycerol (v/v), 100 μg/ml bovine serum albumin and 1 mM β-ME. The LABVIEW software (National

Instrument) was used to select fluorescent bursts induced by single molecules. The FRET efficiency (E) and stoichiometry parameter (S) were calculated as described previously (Lee et al., 2005):

$$E = \frac{I_D^A}{I_D^D + I_D^A}, \quad S = \frac{I_D^D + I_D^A}{I_D^D + I_D^A + I_A^A},$$

where I_D^A (D: donor, A: acceptor) denotes a fluorescent emission of acceptor dye by donor excitation (FRET signal), I_D^D a fluorescent emission of donor dye excited by donor-excitation laser, I_A^A a fluorescent emission of acceptor dye excited by acceptor-excitation laser. The noises were corrected that arise from the leakage (donor emission detected by acceptor detector), the direct acceptor excitation and the intrinsic noise of laser scattering. The ratio of detection efficiency was ~1. The distance between Cy3 and Cy5 was estimated by the equation of $R = R_0(1/E-1)^{1/6}$ with the R_0 value of 6 nm for the Cy3-Cy5 pair (Roy et al., 2008).

For TIRF-FRET analysis, dye-labeled BsSmcH-CC100 was first encapsulated in a lipid vesicle. Synthetic lipids, 1-palmitoyl-2-oleoyl-sn-glycero-3-phosphocholine, 1,2-dioleoyl-sn-glycero-3-[phospho-L-serine], cholesterol, 1-palmitoyl-2-oleoyl-sn-glycero-3-phophoethanolamine and 1,2-Dipalmitoyl-sn-Glycero-3-phosphoethanolamine-N-Biotinyl, were purchased from Avanti Polar Lipids and mixed with molar ratios of 64.9:5:20:10:0.1. After forming large unilamellar vesicles (Kim et al., 2012), extrusion using mini extruder (Avanti Polar Lipids) with 100 nm polycarbonate filter (Whatman) was performed to make mono-disperse unilamellar vesicles. During this process, dye-labeled BsSmcH-CC100 was added for encapsulation inside a vesicle. To ensure one or less than one protein molecule per vesicle for single-molecule detection, the molar ratio of the protein and vesicle was kept approximately 1:100. Unencapsulated protein was removed by a CL-4b column (Sigma). The vesicles were attached onto a quartz glass coated with PEG-biotin and PEG (1:40 mass ratio, Laysan Bio) via Neutravidin (PIERCE). To increase photostability, the flow chamber was washed at each step with an oxygen scavenger buffer containing 20 mM Tris-HCl (pH 7.5), 100 mM NaCl, 1 mM NaN_3 and 1 mM DTT. A prism type TIRF setup based on an inverted microscope (IX71, Olympus) with water-immersion objective (60X, 1.20 NA, UPlanSApo, Olympus) was used for real-time observation. The power of the donor excitation laser (532 nm laser, Cobolt) was

50 μW. The fluorescent emission from the sample was separated into two pathways depending on the wavelength by dual viewer (DV2, Photometrics). A dichroic mirror (FF624, Semrock) was used for dividing donor and acceptor emissions, which were filtered by FF01-580/60 (Semrock) and FF01-675/67 (Semrock), respectively. The images were recorded using an EMCCD (Andor DU-897D) with a 10 frames/sec acquisition speed. The ratio of the detection efficiency (acceptor detection efficiency/donor detection efficiency) was ~1.2 in the TIRF-FRET system. A fluorescence time trace showed a clear one-step acceptor beaching, followed by a donor bleaching, which ensured encapsulation of a single molecule per vesicle.

Anisotropy Titration Measurements.

Fluorescence anisotropy titrations were performed at 25 °C using a BioTek Neo plate reader in a buffer containing 50 mM Tris-HCl at pH 7.5, 50 mM NaCl, and 2-3 mM $MgCl_2$ (+ 1 mM ATP). Anisotropy was measured with the instrument in the T format, allowing simultaneous acquisition of parallel (I//) and perpendicular (I⊥) components. Anisotropy was calculated based upon (Brownbridge et al., 1993).

Total fluorescence intensity (F_t) is given by:

$$F_t = \sum c_i F_i$$

Total anisotropy (A_t) is given by:

$$A_t = \frac{\sum c_i F_i A_i}{F_t}$$

Where c_i is the concentration of species i, F_i is the fluorescence intensity per unit of concentration and A_i is the anisotropy. This is calculated from the parallel and perpendicular fluorescence intensity (I) in relation to the plane of excitation by:

$$A_i = \frac{I_{parallel} - I_{perpendicular}}{I_{parallel} + 2I_{perpendicular}}$$

As anisotropy is additive for multiple fluorescence species in solution, it is used to give a measure of their relative concentrations. For Smc (and various constructs) there are two fluorescence species, DNA and Smc.DNA. The total anisotropy can then be calculated in terms of the dissociation constant (K_D) for the Smc.DNA complex:

$$A_t = \frac{A_{DNA}([DNA]_t - [Smc.DNA]) + A_{Smc.DNA}Q[Smc.DNA]}{[DNA]_t - [Smc.DNA] + Q[Smc.DNA]}$$

Where

$$[Smc.DNA] = \frac{([Smc]_t + [DNA]_t + K_D) - \sqrt{([Smc]_t + [DNA]_t + K_D)^2 - 4[Smc]_t[DNA]_t}}{2}$$

And where $[Smc]_t$ and $[DNA]_t$ are the total concentrations for each reactant. [Smc.DNA] is the concentration of the protein-bound DNA complex. Q is the fluorescence intensity of Smc.DNA relative to DNA. The anisotropy data were fitted to obtain dissociation constants based on the above equations using GraFit fitting software (Leatherbarrow, 2001).

DNA Substrates

Labeled and unlabeled oligonucleotides were purchased from Sigma-Aldrich. To form DNA substrates, oligonucleotides were mixed at equimolar concentrations at 50 µM in either water or a buffer containing 50 mM Tris-HCl at pH 7.5, 150 mM NaCl, and 3 mM $MgCl_2$.

ds40 A TTAGTTGTTCGTAGTGCTCGTCTGGCTCTGGATTACCCGC*
ds40 B GCGGGTAATCCAGAGCCAGACGAGCACTACGAACAACTAA
*is fluorescein

Dynamic light scattering

*Bs*SmcH-CC100(C437S, A715C) protein (6.5 µM) was incubated in 50 mM Tris-HCl, 50 mM NaCl, 2 mM $MgCl_2$, 0.25 mM TCEP, pH 7.5 (final) in the presence or absence of 20 µM DNA (40 bp). Measurements were performed at 20 °C in a DynaPro NanoStar instrument (Wyatt Technologies), analysed with DYNAMICS V7 (Wyatt Technologies) and results from multiple acquisitions were averaged. Mass distributions are shown assuming isotropic spheres.

Cysteine cross-linking and labeling of *Bs*SmcH-CC100

Protein and double stranded oligonucleotides (40 bp) were mixed at 4 µM and 20 µM, respectively, in 50 mM Tris-HCl, 50 mM NaCl, 2 mM $MgCl_2$, 0.25 mM TCEP, pH 7.5 / 23

°C (final). After incubation at room temperature for 5 min, BMOE was added to a final concentration of 0.5 mM from a 20 mM stock solution in DMSO. BM-dPEG$_n$ cross-linkers (Celares GmbH) and Oregon-Green maleimide (Life Technologies) were used at the same concentration. When no maleimide compound was used, an equal volume of DMSO was added. Reactions were incubated for 1 min at room temperature and quenched with 2-mercaptoethanol (14 mM).

Circular dichroism spectroscopy

Data were collected on a JASCO model J-810 spectropolarimeter with a 0.2 cm cuvette. CD spectrum was recorded over the range of 200–250 nm in a nitrogen atmosphere with the *Sc*Smc2H-CC110–*Sc*Smc4H-CC110 protein samples (0.1 mg/ml) dissolved in 40 mM sodium phosphate buffer (pH 7.0) containing 1 mM DTT. The spectrum was the accumulation of three scans corrected by subtracting signals from the buffer control.

Yeast strain construction

Yeast strains are derivatives of *Saccharomyces cerevisiae* W303. Genetic modifications of *SMC2* and *SMC4* loci were done by double crossover recombination. Mutants were selected on synthetic media and maintained on YPAD after single colony purification. Genotypes are listed in Table S2.

Immunoprecipitation and cysteine cross-linking

Yeast was diluted from a stationary phase overnight culture into fresh YPAD to an A_{600} of 0.1. Cells were grown at 30 °C to an A_{600} of approximately 0.8 and harvested by centrifugation, washed in ice cold PBS and snap frozen in PBS supplemented with a protease inhibitor cocktail (Sigma). A concentrated buffer solution was added to each pellet adjusting the conditions to 85 mM sodium phosphate (pH 7.4), 120 mM NaCl, 1 mM EDTA and 14 mM β-ME. Frozen material was broken in a swing mill, quickly thawed and centrifuged for 2 x 10 min at 21,000 x g. The protein extract was incubated for 30 min at 4 °C with Dynabeads Protein G (Life Technologies) charged with monoclonal SV5-Pk1 antibody (AbD Serotec). Beads were washed twice in ice cold PBS, then resuspended in PBS. BMOE was added to a final concentration of 0.5 mM from a 20 mM stock solution in DMSO. When no cross-linker was used, an equal amount of DMSO was

added. Reactions were incubated for 10 min on ice before quenching with 2-ME at a final concentration of 14 mM. Beads were incubated for 15 min at 37 °C in PBS supplemented with protease inhibitors and 5 µM HaloTag TMR substrate (Promega) before boiling in SDS-PAGE sample buffer. Gels were analyzed on a Typhoon scanner (GE Healthcare) with Cy3 DIGE setup.

Immunoblot analysis

Yeast was grown as described above, washed once in PBS and then resuspended in 10 % (w/v) trichloroacetic acid followed by mechanical cell lysis and collection of precipitated protein by centrifugation. Electroblots were probed with SV5-Pk1 antibodies at a dilution of 1:2,000.

Construction of *Bs*Smc*Tm*H and suppressor mutagenesis

The chimeric Smc protein, *Bs*Smc*Tm*H, was constructed starting from a *Bs smc* targeting vector (pSG001) by replacing the *Bs smc* fragment encoding aa495-678 by the corresponding fragment of *Thermotoga maritima* MSB8 *smc*, aa491-670 (pSG1167). Random mutations in the *Tm* part of BsSmcTmH were generated by cloning of *Taq* polymerase amplified PCR products into the parental vector. A *smc* mutant lacking the hinge domain (BSG1306) was transformed with the cloned DNA library. Transformants were selected for growth on rich medium, *i.e.* nutrient agar, streaked for single colonies and characterized by PCR and sequencing. Selected mutations were cloned and re-transformed to ensure a clean genetic background.

Electrostatic surface potential for Smc hinge

A structural homology model for the *Bs* Smc hinge domain was generated based on the *Tm* Smc hinge coordinates (PDB: 1GXL) using Modeller software (Eswar et al., 2007) with default settings. Electrostatic surface potential maps were calculated using a APBS plugin in Pymol and displayed in Pymol at ± 6 kT/e (Baker et al., 2001).

SUPPLEMENTAL REFERENCES

Baker, N.A., Sept, D., Joseph, S., Holst, M.J., and McCammon, J.A. (2001). Electrostatics of nanosystems: application to microtubules and the ribosome. Proceedings of the National Academy of Sciences of the United States of America *98*, 10037-10041.

Brownbridge, G.G., Lowe, P.N., Moore, K.J., Skinner, R.H., and Webb, M.R. (1993). Interaction of GTPase activating proteins (GAPs) with p21ras measured by a novel fluorescence anisotropy method. Essential role of Arg-903 of GAP in activation of GTP hydrolysis on p21ras. The Journal of biological chemistry *268*, 10914-10919.

Brunger, A.T., Adams, P.D., Clore, G.M., DeLano, W.L., Gros, P., Grosse-Kunstleve, R.W., Jiang, J.-S., Kuszewski, J., Nilges, M., and Pannu, N.S. (1998). Crystallography & NMR system: A new software suite for macromolecular structure determination. Acta Crystallogr. D Biol. Crystallogr. *54*, 905-921.

Emsley, P., and Cowtan, K. (2004). Coot: model-building tools for molecular graphics. Acta Crystallogr. D Biol. Crystallogr. *60*, 2126-2132.

Eswar, N., Webb, B., Marti-Renom, M.A., Madhusudhan, M.S., Eramian, D., Shen, M.Y., Pieper, U., and Sali, A. (2007). Comparative protein structure modeling using MODELLER. Current protocols in protein science / editorial board, John E. Coligan ... [et al.] *Chapter 2*, Unit 2 9.

Franke, D., and Svergun, D.I. (2009). DAMMIF, a program for rapid ab-initio shape determination in small-angle scattering. J. Appl. Cryst. *42*, 342-346.

Fuentes-Perez, M.E., Gwynn, E.J., Dillingham, M.S., and Moreno-Herrero, F. (2012). Using DNA as a fiducial marker to study SMC complex interactions with the atomic force microscope. Biophysical journal *102*, 839-848.

Kim, J.-Y., Choi, B.-K., Choi, M.-G., Kim, S.-A., Lai, Y., Shin, Y.-K., and Lee, N.K. (2012). Solution single-vesicle assay reveals PIP2-mediated sequential actions of synaptotagmin-1 on SNAREs. EMBO J. *31*, 2144-2155.

Kozin, M.B., and Svergun, D.I. (2001). Automated matching of high-and low-resolution structural models. J. Appl. Cryst. *34*, 33-41.

Lee, N.K., Kapanidis, A.N., Wang, Y., Michalet, X., Mukhopadhyay, J., Ebright, R.H., and Weiss, S. (2005). Accurate FRET measurements within single diffusing biomolecules using alternating-laser excitation. Biophys. J. *88*, 2939-2953.

McCoy, A.J., Grosse-Kunstleve, R.W., Adams, P.D., Winn, M.D., Storoni, L.C., and Read, R.J. (2007). Phaser crystallographic software. J Appl Cryst *40*, 658-674.

Mitov, M.I., Greaser, M.L., and Campbell, K.S. (2009). GelBandFitter--a computer program for analysis of closely spaced electrophoretic and immunoblotted bands. Electrophoresis *30*, 848-851.

Otwinowski, Z., and Minor, W. (1997). Processing of X-ray diffraction data. Methods Enzymol. *276*, 307-326.

Rambo, R.P., and Tainer, J.A. (2013). Accurate assessment of mass, models and resolution by small-angle scattering. Nature *496*, 477-481.

Roy, R., Hohng, S., and Ha, T. (2008). A practical guide to single-molecule FRET. Nat. Methods *5*, 507-516.

Shen, A., Lupardus, P.J., Morell, M., Ponder, E.L., Sadaghiani, A.M., Garcia, K.C., and Bogyo, M. (2009). Simplified, enhanced protein purification using an inducible, autoprocessing enzyme tag. PloS one *4*, e8119.

Volkov, V.V., and Svergun, D.I. (2003). Uniqueness of ab initio shape determination in small-angle scattering. J. Appl. Cryst. *36*, 860-864.